TWO-WAVELENGTH LIDAR INSTRUMENT FOR ATMOSPHERIC AEROSOL STUDY

by

David Swick Hoffman

A thesis submitted in partial fulfillment
of the requirements for the degree

of

Master of Science

in

Electrical Engineering

MONTANA STATE UNIVERSITY
Bozeman, Montana

April, 2008

APPROVAL

of a thesis submitted by

David Swick Hoffman

This thesis has been read by each member of the thesis committee and has been found to be satisfactory regarding content, English usage, format, citations, bibliographic style, and consistency, and is ready for submission to the Division of Graduate Education.

Dr. Kevin S. Repasky

Approved for the Department of Electrical and Computer Engineering

Dr. Robert C. Maher

Approved for the Division of Graduate Education

Dr. Carl A. Fox

STATEMENT OF PERMISSION TO USE

In presenting this thesis in partial fulfullment of the requirements for a master's degree at Montana State University, I agree that the Library shall make it available to borrowers under rules of the Library.

If I have indicated my intention to copyright this thesis by including a copyright notice page, copying is allowable only for scholarly purposes, consistent with "fair use" as prescribed in the U.S. Copyright Law. Requests for permission for extended quotation from or reproduction of this thesis in whole or in parts may be granted only by the copyright holder.

David Swick Hoffman

April, 2008

ACKNOWLEDGEMENTS

I would like to thank my adviser, Dr. Kevin Repasky, for allowing me to work on this project and for helping me complete it. I would also like to thank my other committee members Dr. John Carlsten and Dr. Robert Maher who were instrumental in addressing possible sources of error and other concerns. Finally, I would like to thank Seth Humphries for helping me type-set this thesis using Latex. This work was supported by NASA grant number NNX06AD11G, and by a fellowship from the Montana Space Grant Consortium. The CALIPSO satellite data presented in this thesis were obtained from the NASA Langley Research Center Atmospheric Science Data Center.

TABLE OF CONTENTS

TABLE OF CONTENTS – CONTINUED

LIST OF TABLES

LIST OF FIGURES

Figure Page

LIST OF FIGURES – CONTINUED

Figure Page

LIST OF FIGURES – CONTINUED

Figure Page

LIST OF FIGURES – CONTINUED

Figure Page

ABSTRACT

A two-color lidar instrument and inversion algorithms have been developed for the study of atmospheric aerosols. The two-color lidar laser transmitter is based on the collinear fundamental 1064 nm and second harmonic 532 nm output of a Nd:YAG laser. Scattered light is collected by the two-color lidar receiver using a Schmidt-Cassegrain telescope with the 532 nm channel monitored using a gated photomultiplier tube (PMT) and the 1064 nm channel monitored using an avalanche photodiode (APD). Data is collected from the PMT and APD using a 14 bit 200 MHz data acquisition card. The lidar inversion algorithm developed to analyze the data collected by the two-color lidar is based on a constant lidar ratio assumption at both the 1064 nm and 532 nm wavelengths with the constrained ratio aerosol model (CRAM) providing the initial lidar ratios at the two wavelengths to complete the lidar inversion. Data from the CALIOP lidar on board the CALIPSO satellite are presented to verify software algorithm performance. Data from the two-color lidar are then presented demonstrating the two-color lidar instrument's capabilities. The analysis of these data identifies smoke and industrial aerosols in the atmosphere above Bozeman. Finally an error analysis of the lidar instrument and accompanying analysis software is presented. The findings of this analysis are that error introduced by the APD and PMT is dominant; the error introduced by the optical detectors is much larger than the error from other sources examined such as quantization error, and the error associated the use of numerical integration in the data analysis algorithm.

1

INTRODUCTION

This thesis presents a two-wavelength lidar instrument, built for the purpose of atmospheric aerosol study, as well as data analysis software algorithms and example lidar data. Work done in support of this thesis includes the design and construction of the two wavelength lidar instrument, the development of data analysis software and the analysis of lidar data obtained using the two wavelength lidar instrument. Additionally, lidar data from the CALIOP lidar instrument on board the CALIPSO satellite was analyzed to provide evidence supporting the validity of the data analysis software.

Atmospheric Aerosols

Atmospheric aerosols are widely understood to play a significant role in the planetary radiation budget; however, there are still many unknowns surrounding the radiative forcing (the affect on the local radiation-energy budget) of aerosols (for more information of radiative forcing see [1]). The direct and indirect forcing effects of aerosols each influence the global climate significantly and both need to be better understood in order to create accurate world climate models [1]. Direct radiative forcing is caused by the scattering and absorption of incoming solar radiation by atmospheric aerosols. The direct effects of aerosol absorption are strongly dependent on altitude and geographic location, meaning that ground sampling of aerosols often can provide misleading information about their overall radiative forcing [1]. Absorbing aerosols in the upper atmosphere over dark surfaces such as large bodies of water produce a negative forcing, while the same aerosols over a lighter surface such as a snow-field, or simply positioned lower in the atmosphere will produce a

positive forcing. Scattering aerosols generally produce a negative radiative forcing [1]. The complexity of the direct radiative forcing effects, compounded by the short atmospheric lifetime of aerosols, clearly demonstrates the need for more study of aerosols and their radiative forcing.

Cloud-aerosol microphysical interactions make up the most significant aerosol radiative indirect effects. These interactions affect cloud formation, lifetime, albedo and other properties. For example, the interaction between airborne pollution from Asia and convective cloud formation above the Pacific Ocean has been shown to cause increased intensity of Pacific storms [2]. The most significant aerosol indirect radiative forcing is caused by the effect of aerosols on cloud albedo [3]. As of the publication of the latest Intergovernmental Panel on Climate Change report, radiative forcing due to aerosol induced changes in cloud albedo varied widely from $-.22$ to $-2.00[W/m^2]$ [1]. The effects of different aerosols on cloud albedo are highly dependent on both the concentration and the chemical properties of the aerosols in question [4]. The cloud albedo related indirect forcing effects of aerosols are a large source of uncertainty in global climate models [1].

Aerosol concentrations can change rapidly and their forcing effects are highly dependent on aerosol species, geographic location and altitude [2]. The radiative forcing of aerosols is one of the largest sources of error and uncertainty in current climate models [1]. New studies are needed to learn more about global aerosol distributions and radiative forcing. Such studies could improve the accuracy of future global climate models. It is therefore very important to develop new instrumentation for altitude-resolved study and tracking of atmospheric aerosols.

Lidar

Lidar (Light Detection and Ranging) involves illuminating a target (in this case the atmosphere) with light and observing the light that is scattered back in order to gain information about that target. Depending on the nature of the lidar instrument being used, different features of the target of interest can be observed either directly or indirectly. For example, the distance to an object can be measured by observing the time taken by light to travel to the object, be reflected, and travel back to the lidar instrument as illustrated in Figure 1. Lasers are a commonly used light source in lidar systems because they enable spatially, temporally and spectrally precise illumination of a desired target. By observing the temporal and spectral distribution as well as the intensity of the light that is backscattered, inferences can be made about physical and chemical properties of the target. For example, by observing the difference between the wavelength of the light source and the Doppler-shifted backscattered light from a moving target, inferences can be made about the motion of that target relative to the lidar system [5]. Additionally, a multi-wavelength lidar system can determine atmospheric characteristics by observing how the atmosphere interacts with different wavelengths of light.

Lidar Equation

The backscattered light received by a lidar system at any given time can be represented as a function of the light transmitted by the lidar attenuated by various factors and delayed by the round-trip travel time of that light. The basic lidar equation describes the optical power received by the lidar instrument, $P_\lambda(r)$, from

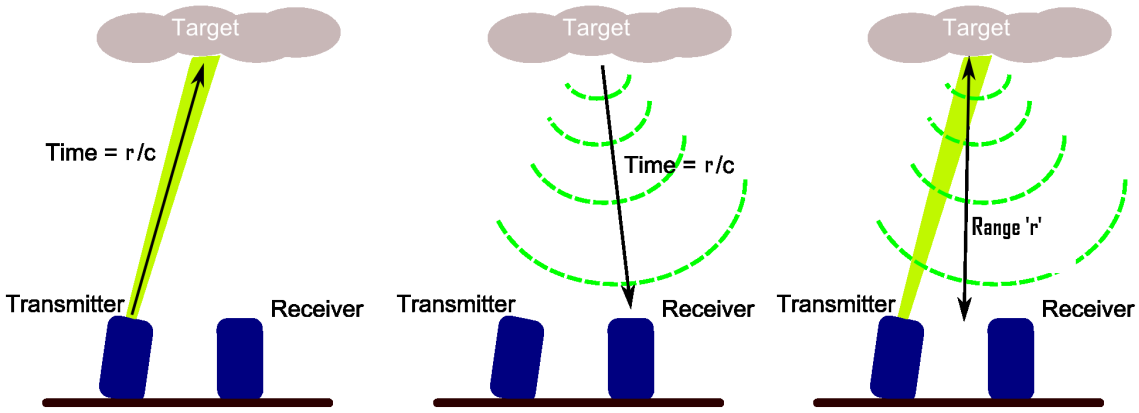

Figure 1: A basic lidar system diagram. If a pulse of light is emitted from the transmitter, it will take r/c time to travel to a target at range r and another r/c for light scattered by the target to reach the receiver, where c is the speed at which light travels through the atmosphere. It will therefor take $2r/c$ time for the total round trip of the light. The range to the target can then be calculated by $r = \frac{total\ time}{2c}$.

a range of r [5]

$$P(r) = P_t \frac{A}{r^2} \frac{c\tau}{2} \beta(r) e^{-2 \int_0^r \sigma(r')dr'} \epsilon(\lambda)\epsilon(r), \tag{1}$$

where P_t is the laser transmitter pulse power, A is the area of the lidar receiver's light collection optics, c is the speed of light, τ is the laser pulse duration, $\beta(r)$ is the backscatter coefficient, $\sigma(r)$ is the extinction coefficient, $\epsilon(\lambda)$ is the spectral transmission of the receiver optics at wavelength λ and $\epsilon(r)$ is the overlap function. The overlap function, $\epsilon(r)$, refers to the overlap between the field of view of the telescope and the intensity profile of the laser as a function of range. The extinction coefficient, $\sigma(r)$, represents the amount of light emitted by the lidar system that experiences scattering, absorption, or other phenomena at range r that prevents it from propagating to further ranges. The integration of the extinction coefficient from range 0 to range r multiplied by 2 represents the total amount of light absorbed, scattered, or otherwise impeded while traveling from the lidar instrument to range

r and back again. Taking this factor into account allows for meaningful study of a particular range, while eliminating as much as possible the influences of conditions between the lidar system and that specific range. The backscatter term, $\beta(r)$, represents the light scattered at range r in a backward direction such that the light is sent back toward the lidar instrument.

Lidar is a useful tool for studying aerosols because many prevalent aerosol species can be readily identified by their extinction and backscatter properties at multiple wavelengths. Properly calibrated multi-wavelength lidar instruments are capable of making range-resolved measurements of extinction and backscatter, making them ideal for studying atmospheric aerosols.

6

THE TWO WAVELENGTH LIDAR INSTRUMENT

The design of the lidar instrument presented in this paper is based on the author's design of several previous lidar systems (for example, see [6]), with several key exceptions. The lidar instrument presented here makes use of two wavelengths of light, and is specifically designed to study atmospheric aerosols. Important design considerations specific to aerosol study are that the laser beam and the telescope field of view are fully overlapped (the laser beam transverse energy profile fits within the telescope field of view) at ranges where aerosols are to be studied, and that each detector (there is one detector for each of the two wavelengths of light) sees the same field of view. Additionally, the vertical resolution, which is determined primarily by the laser pulse-width, should be small enough to reasonably observe atmospheric aerosols. Given the often thin vertical extent of aerosol plumes, resolution of 10 meters or less is desired (corresponding to a pulse width of 60 ns or shorter). Other design parameters of note are that the laser should emit enough energy per pulse to adequately illuminate the atmosphere, and that background light from the sky is somehow prevented (as much as possible) from striking the optical detectors. A Nd:YAG laser was chosen as the light source for the two-wavelength lidar instrument because fundamental and second harmonic frequencies emitted by such a laser are adequate for studying atmospheric aerosols (there are tables of known aerosol optical properties corresponding to similar wavelengths), and because Nd:YAG lasers and optical components optimized for their first and second harmonic wavelengths are relatively easy and economical to obtain.

Laser Transmitter

A schematic of the two-color lidar instrument is shown in Figure 2. A Nd:YAG laser is used to produce light at the fundamental 1064 nm and second harmonic 532 nm wavelengths. The flash-lamp pumped Q-switched laser produces laser pulses of approximately 9.9 ns with a pulse repetition frequency (PRF) of 20 Hz. The pulse energy at the fundamental (second harmonic) wavelength is 50 mJ (100 mJ). The laser beams exit the laser collinearly with a beam diameter of 0.54 cm. The beams are next expanded and re-collimated using a diverging lens with a focal length of -2.5 cm, then a converging lens with a focal length of 10 cm. After the second lens, the collimated light has a beam diameter of 2.7 cm. The collimated light is next incident on a dielectric mirror that directs most of the collinear fundamental and second harmonic light into the atmosphere. The small amount of the fundamental and second harmonic light passing through this dielectric mirror is incident on a second dielectric mirror that reflects the fundamental 1064 nm light but allows the second harmonic 532 nm light to be transmitted. The reflected fundamental frequency light is then incident on an energy detector used to monitor the pulse energy of the outgoing 1064 nm beam while the transmitted second harmonic light is incident on a second energy detector used to monitor the outgoing 532 nm pulse energy.

Receiver

The optical receiver for the two-color lidar instrument uses a 28 cm diameter Schmidt-Cassegrain telescope to collect the light scattered by the atmosphere. Since the optical power received by a lidar system is proportional to the physical area of the light collection optics, using as large a telescope as practicable is advantageous. An

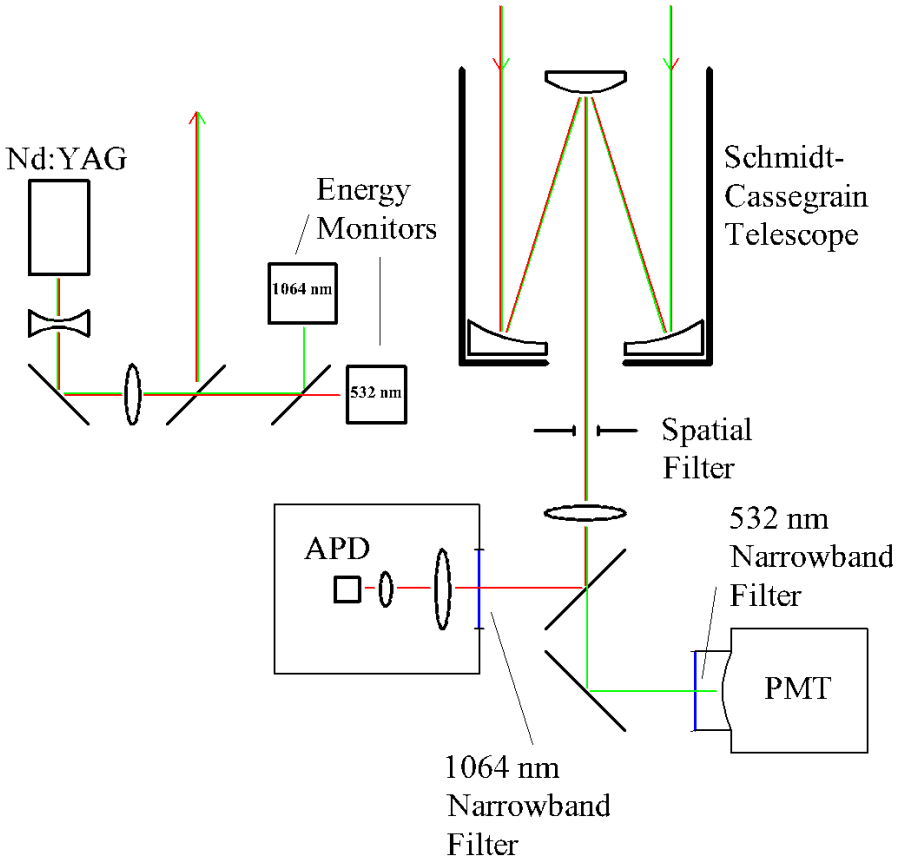

Figure 2: Laser transmitter and receiver optics for the two-color lidar instrument. The laser transmitter is based on a commercial frequency doubled Nd:YAG that emits the fundamental 1064 nm and frequency doubled 532 nm wavelengths. A gated PMT is used to monitor the 532 nm channel while an APD is used to monitor the 1064 nm channel. A Schmidt-Cassegrain telescope is used to collect the backscattered light.

iris, placed at the focal plane of the telescope, is used to reduce the field of view of the telescope to 2 mrad, approximately three times larger than the 0.65 mrad divergence angle of the beams leaving the laser transmitter. The field of view of the telescope must be small to minimize the background light and light that has experienced multiple scattering, but must be larger than the divergence angle associated with the laser transmitter to ensure overlap of the laser transmitter and optical receiver field of view. Light passing through the iris is next collimated using a 5.08 cm diameter lens with a focal length of 10 cm. The collimated light is incident on a dielectric mirror that reflects the fundamental 1064 nm light but transmits the second harmonic 532 nm light. The reflected fundamental 1064 nm light passes through a narrowband optical filter centered at 1064 nm with a 3 nm full width at half maximum (FWHM) pass-band. Two lenses with focal lengths of 2.5 cm and 0.5 cm placed approximately 2.2 cm apart are then used to focus the 1064 nm light onto the 1 mm^2 active area of an avalanche photodiode (APD). The APD is mounted in a TO-can package that is housed in an aluminum light-tight box that contains the two focusing lenses with the narrowband filter placed at the entrance to the light tight-box. A thermo-electric cooler (TEC) is used to control the operating temperature of the APD at 5° C during instrument operation. The transmitted second harmonic 532 nm light that passes through the dielectric mirror is next incident on a narrowband filter centered at 532 nm with a 1 nm FWHM band-pass. After the narrowband filter, the 532 nm light is incident on a gated photomultiplier tube (PMT) module (Hamamatsu H7680-1).

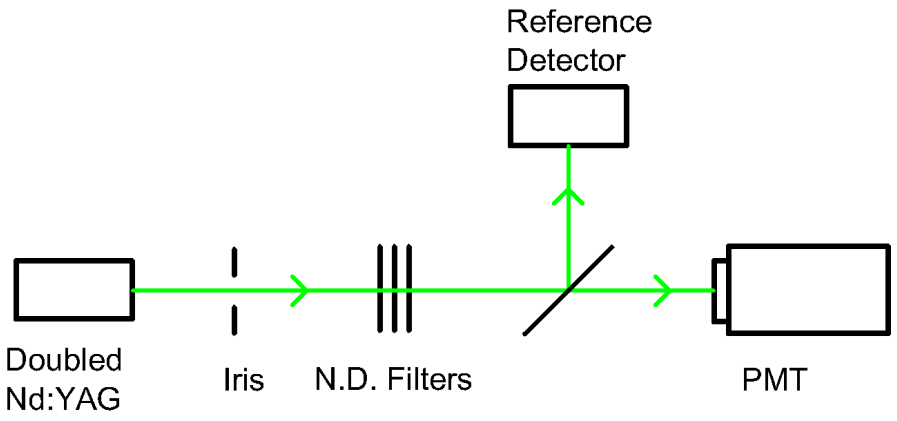

Figure 3: The PMT was characterized using this layout. The transmission and reflectivity of the beam splitter was known a priori, allowing the calculation of the light incident on the PMT using reference measurements. Different combinations of neutral density (N.D.) filters were used to adjust the intensity of the light incident on the PMT. The PMT gain was modulated using the internal gating circuit allowing easy monitoring of its response.

Characterization of Optics and Detectors

PMT Characterization

The PMT used in the two-wavelength lidar instrument has been characterized using the setup shown in Figure 3 to determine its responsivity. Two inputs are used to control the PMT; one signal controls the gain and one controls the gating circuit. The internal high-voltage supply used to power the PMT is controlled by an external signal that can range from 2 V to 5 V. A simple circuit module has been built (see Figure 4) to allow this control voltage to be manually adjusted. This circuit also monitors the PMT for overlight and other error conditions and illuminates warning LED's accordingly. The gating circuit control is a simple TTL (Transistor-Transistor Logic) input that controls the state of the PMT's internal gating circuit. The gating circuit can very rapidly switch the gain of the PMT between the value corresponding to the input control signal and nearly zero (the fall time is 20 ns, the rise time is 10

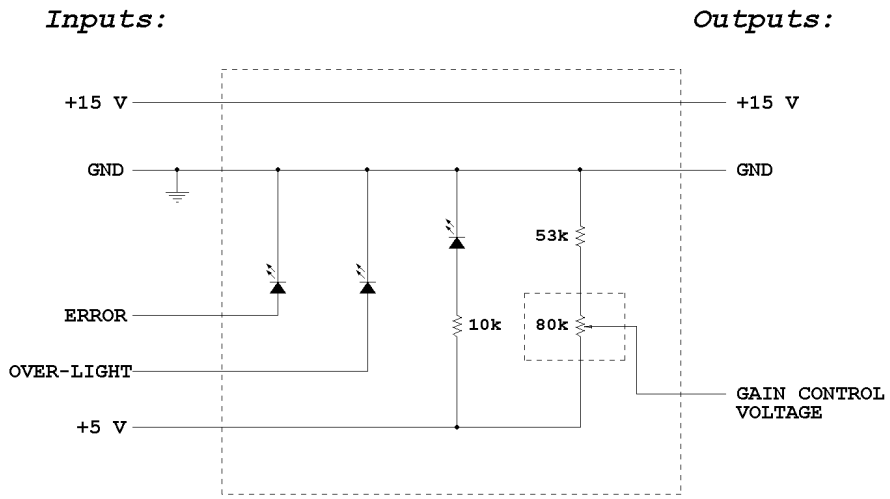

Figure 4: The driver-circuit for the gated PMT module. The +15 V and ground inputs are from a power supply, while the other inputs come from the PMT module. All of the outputs are connected to the PMT module.

ns).

It was determined during initial characterization attempts that the response of the PMT to pulsed light with a relatively large duty cycle (above about 1%, such as that resulting from the use of a mechanical chopper-wheel to modulate the light source) is highly dependent on the duty cycle of the incident light. This is because the PMT was not able to adequately recover in bettween pulses, causing the signal current to be reduced as the duty cycle of the incident light was increased. To avoid this problem, and to as closely as practicable simulate the actual conditions encountered by the PMT during use in the lidar instrument, the PMT's internal gating circuit was used to modulate the signal from the incident light. The gate was driven by an arbitrary function generator at 20 Hz (corresponding to the actual repetition rate of the laser in the lidar instrument) with a 0.5% duty cycle. Under these conditions, the amplitude of the output waveform from the PMT was seen to be unaffected by small changes in the duty cycle of the internal gate. The intensity of the light incident on

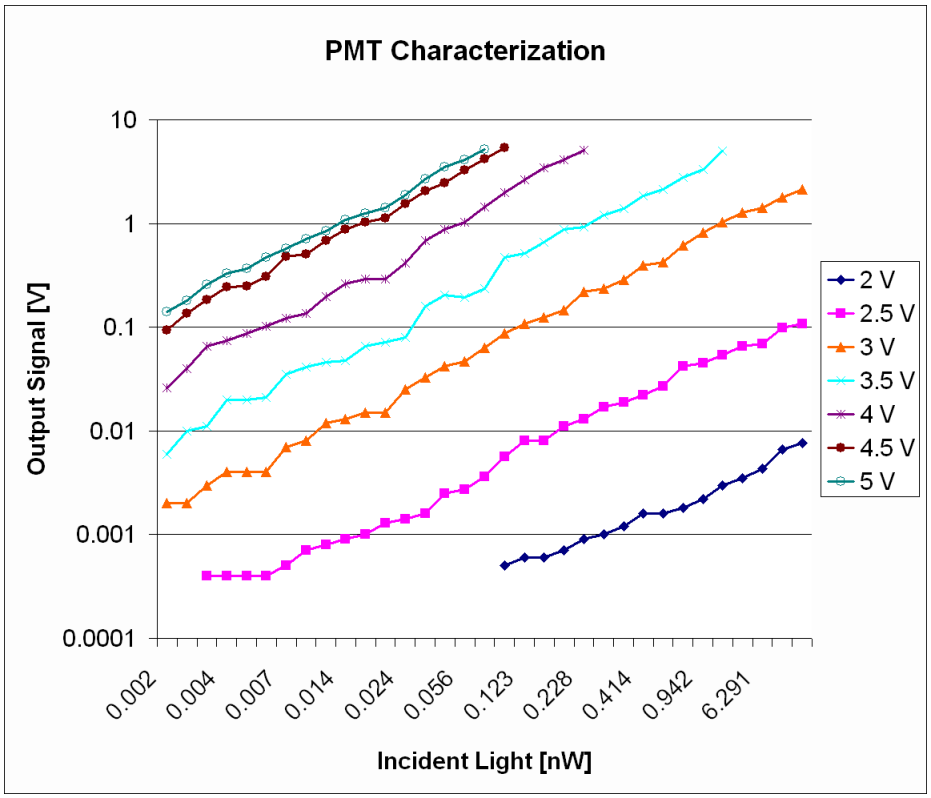

Figure 5: The responsivity of the PMT has been plotted as a function of incident optical power and PMT gain setting. Each data set was recorded using a different gain control voltage varying from 2 V to 5 V in increments of 0.5 V. The "Output Signal" axis is plotted on a logarithmic scale.

the PMT was varied from 1.5 μW to 21 nW for PMT gain settings of 2 through 5 at increments of 0.5, except in cases where the output voltage of the PMT exceeded safe levels. The results of this characterization are plotted in Figure 5 and can be seen in tabular form in Appendix A.

APD Characterization

The APD was characterized in a manner similar to that used for the PMT, with several exceptions. The response of the APD was seen to be independent of the duty cycle of modulated incident light. The APD was therefore characterized using a mechanical chopper-wheel to modulate the incident light. Further, the temperature

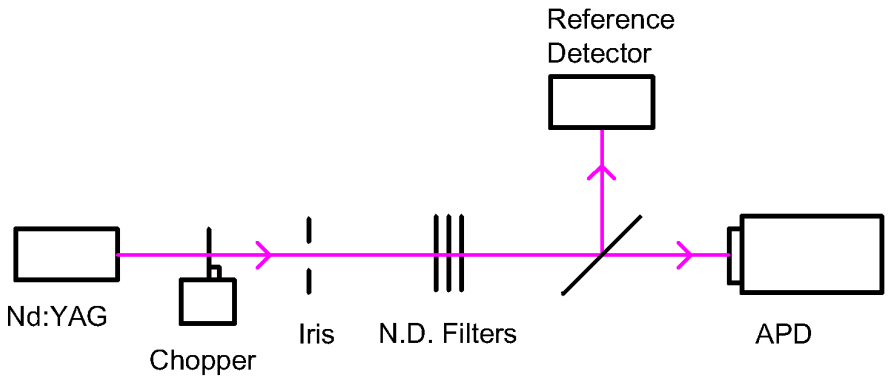

Figure 6: The APD was characterized using this layout. The transmission and reflectivity of the beam splitter was known a priori, allowing the calculation of the light incident on the APD using reference measurements. Different combinations of N.D. filters and laser power settings were used to adjust the intensity of the light incident on the APD. A chopper wheel was used to modulate the light incident on the APD into an approximate squarewave facilitating easy measurement of its response.

of the APD had to be carefully controlled because its gain is strongly dependent on temperature. Rather than characterizing the APD over a range of temperatures, the APD was maintained at a single temperature throughout its characterization and later use in the lidar instrument. Finally, the APD has a fixed gain, allowing it to be characterized with fewer measurements than the PMT. A schematic of the APD characterization setup is shown in Figure 6. The results of the characterization of the APD are plotted in Figure 7, and are displayed in tabular form in appendix A.

Receiver Optics Characterization

The transmission of the optics that collect scattered light from the atmosphere and direct it onto the two detectors in the lidar instrument is an important parameter that is needed for an initial coarse calibration of the lidar instrument as well as for signal to noise calculations. Refractive elements have been characterized in terms of transmission at 532 nm, 1064 nm or both depending on their location and purpose.

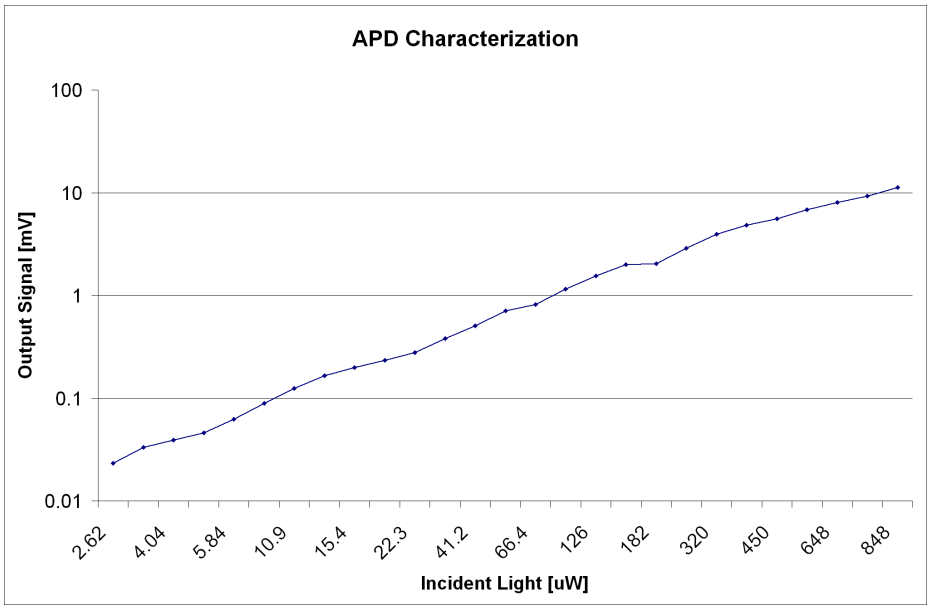

Figure 7: The responsivity of the APD has been plotted as a function of incident optical power. The gain of the APD highly dependent on temperature. It was therefore maintained at 10°C during characterization and later data collection

The lens characterization data are shown in table 1, including the telescope, which was characterized according to its total transmission at each wavelength. The lenses were characterized using the layout shown in Figure 9. Reflective elements have been characterized in terms of reflectivity and transmission at 532 nm, 1064 nm or both depending on their location in the lidar instrument. The mirror characterization data are shown in table 1. The mirrors were characterized using the layout shown in Figure 8. The actual position in the lidar instrument of the lenses and mirrors described in table 1 can be identified by their reference numbers in Figure 10 (i.e. lens 1 in the table matches lens 1 in the Figure 10).

Transmitter Optics Characterization

The optics on the laser transmitter side of the lidar instrument have been characterized such that the outgoing energy of each laser pulse can be monitored.

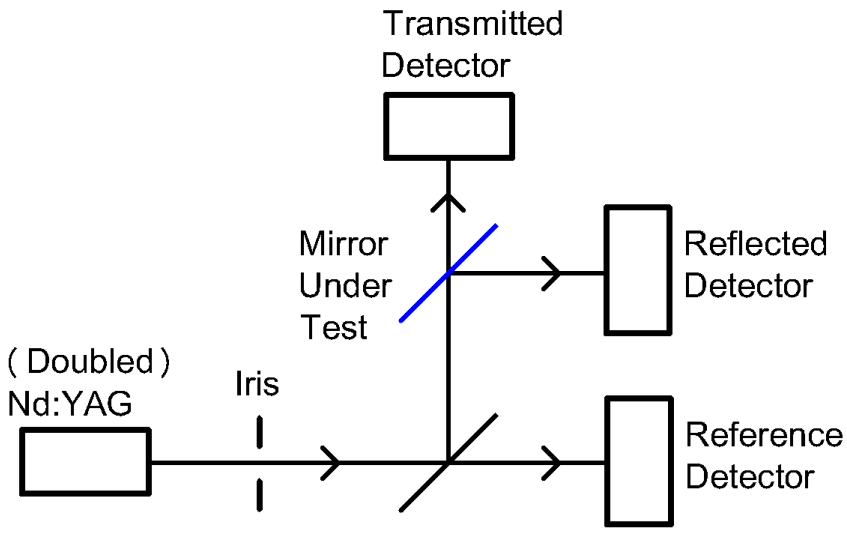

Figure 8: A schematic showing the setup used to characterize the mirrors used in the two-wavelength lidar instrument.

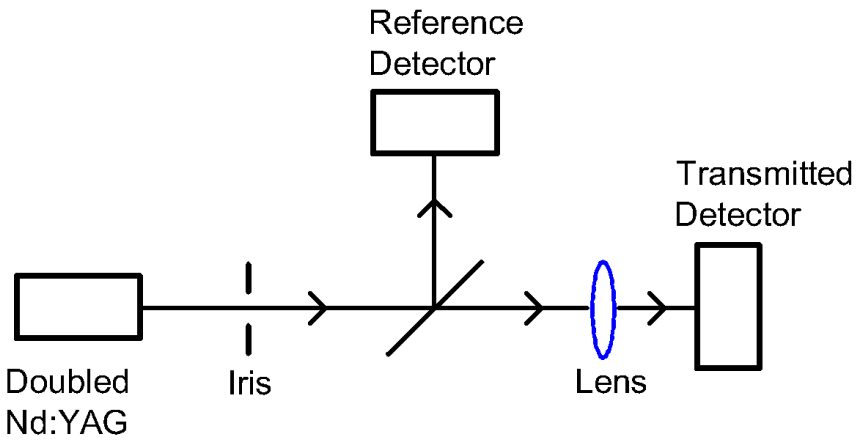

Figure 9: A schematic showing the setup used to characterize the lenses used in the two-wavelength lidar instrument.

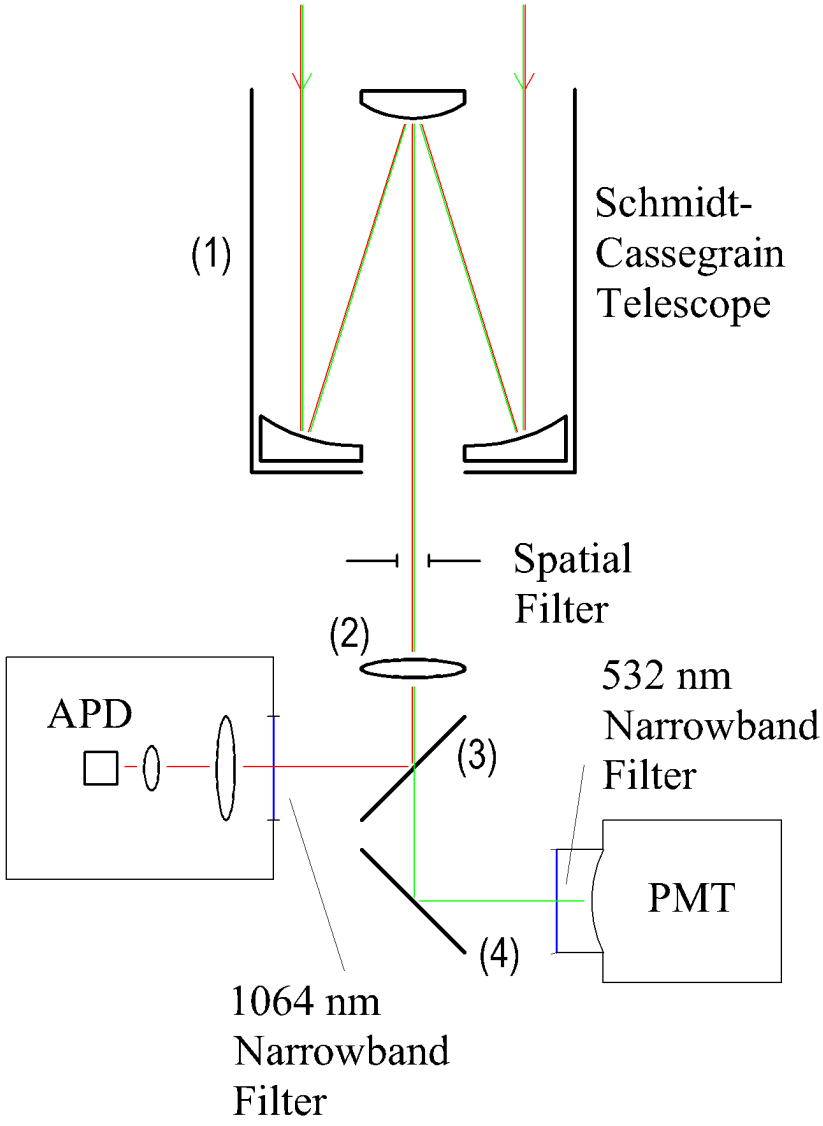

Figure 10: A schematic of the receiver stage of the lidar instrument identifying the optics described in table 1 by their reference numbers.

Table 1: Characterization data for input optics. The reference numbers correspond to the reference numbers in Figure 10. The blank entries correspond to measurements that were not necessary for characterization.

Reference Number	532 nm Transmission	1064 nm Transmission	532 nm Reflectivity	1064 nm Reflectivity
1	85.26%	63.76%		
2	92.75%	94.58%	7.25%	5.42%
3	78.88%		7.9%	99.20%
4			97.7%	98.3%

Table 2: Characterization data for output optics. The reference numbers correspond to the reference numbers in Figure 11.

Mirror Reference Number	532 nm Transmission	1064 nm Transmission	532 nm Reflectivity	1064 nm Reflectivity
1	0.01%	0.01%	93.6%	97.2%
2	91.4%	0.02%	7.9%	98.3%

This requires knowledge of the reflectivity and transmission at each wavelength of the the final turning mirror as well as the mirror that splits the reference light into two channels for monitoring each wavelength. Because the energy measurement is made after the first turning mirror and the expansion optics, these elements have not been carefully characterized; they have instead been checked to ensure that they are adequately executing their intended purpose. The characterization data for the transmitter optics are shown in table 2. The optics described in the table can be located according to reference number in Figure 11. These optics were characterized using the layout shown in Figure 8.

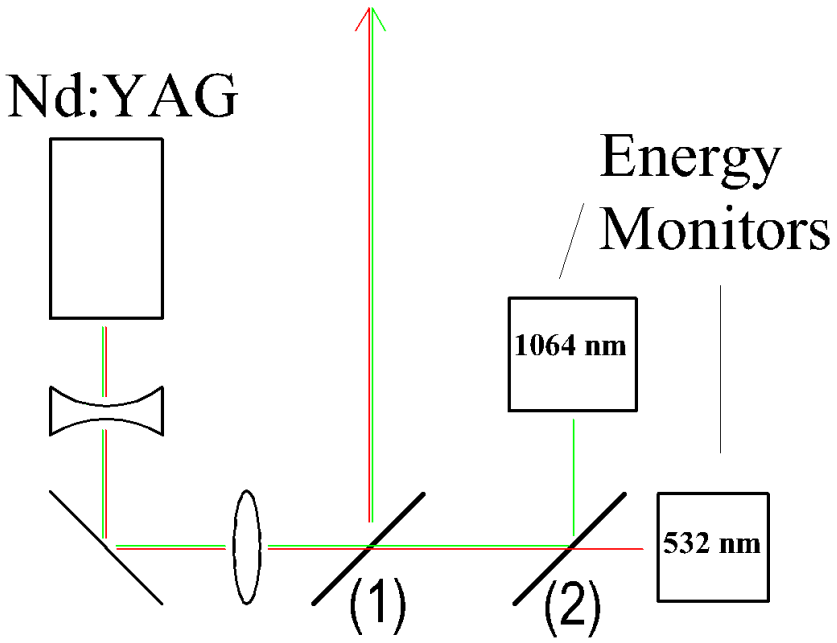

Figure 11: A schematic of the transmitter stage of the lidar instrument identifying the optics described in table 2 by their reference numbers.

METHODS: DATA COLLECTION AND ANALYSIS

Data Collection

The electrical signals from the APD and PMT assemblies are digitized using a 14 bit 200 MHz A/D converter. This leads to 0.75 m vertical range bins. However, the 9.9 ns laser pulse width results in a vertical resolution of 1.5 m. The raw signal from the A/D converter is too noisy to be used to perform an inversion. The main sources of noise include ambient light from the atmosphere and electrical noise from the Q-switch in the laser and the gating circuit in the PMT. The noise from the Q-switch and gating circuit vary over the course of each lidar return, while the ambient light varies over the course of a whole data collection run consisting of many lidar returns. To measure all of these sources simultaneously, every alternate lidar return for each wavelength is recorded with the laser's internal shutter closed. The noise measurements are then digitally subtracted from the previously recorded lidar return. Due to limitations of the A/D converter, the 532 nm and 1064 nm returns must be measured sequentially rather than simultaneously. Data is therefore collected in the following manner: A time resolved voltage signal from the gated PMT is recorded for the 532 nm first laser pulse. Next, a time resolved voltage signal is recorded for the 1064 nm channel for a second laser pulse. An internal shutter is then closed within the laser via the computer and a third time resolved voltage signal from the gated PMT is collected. Finally, with the shutter still closed, a time resolved voltage signal from the APD is collected. The background signal taken with the closed shutter is then subtracted from the return signal to remove the background noise on a shot by shot basis with the resulting signals stored in a data file. Thus, four laser pulses are required to produce a background-subtracted return from both the 1064 nm and 532

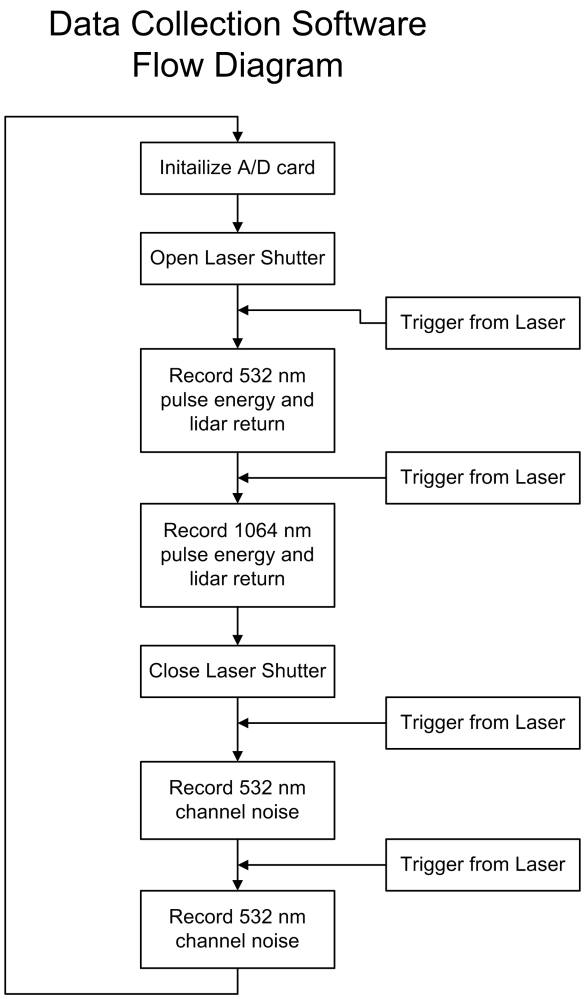

Figure 12: A flow diagram of the data acquisition process, which is carried out using Labview (tm) software.

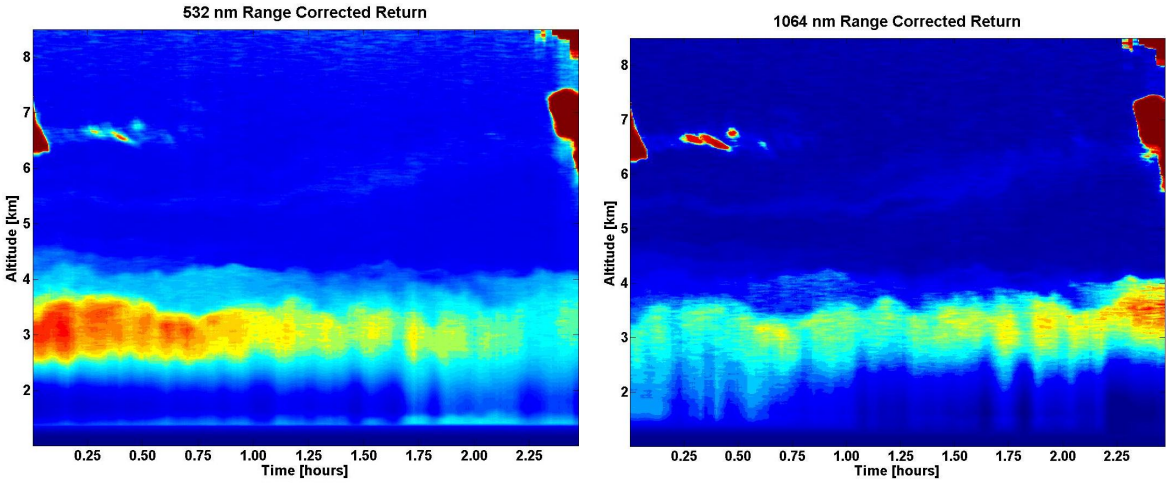

Figure 13: Data acquired from the 532 nm and 1064 nm channels of the two-color lidar instrument at Montana State University during a nearby forest fire event (red corresponds to the highest return, blue to the lowest). A plume of smoke is clearly visible at approximately 3 km. The darker objects above the plume to the sides of the plots are clouds.

nm channels. Since the PRF of the laser is 20 Hz, this means that a background-subtracted return signal collected for both channels occurs every 0.2 s. This process is repeated for a user defined time. This data acquisition process utilizes Labview (tm) software to store the data that is digitized by the A/D card, read the energy meters and control the laser shutter. A flow chart describing the data acquisition process is shown in figure 12. Samples of the data collected from the 532 nm and 1064 nm channels of the two-color lidar are shown in figure 13. These false color plots show the range corrected return signal as a function of altitude and time. The range corrected return signal is found by multiplying the actual return signal by the square of the altitude to eliminate the altitude dependence of the return signal.

Data Processing

The data processing algorithm used to process data collected by the two color lidar instrument developed at Montana State University utilizes the inversion techniques developed by Fernald et al. [7] for a two component atmosphere. Taking into account multiple transmitter wavelengths, eqn(1) can be re-written as

$$P_\lambda(r) = P_{t,\lambda}\frac{A}{r^2}\frac{c\tau}{2}\beta(\lambda,r)e^{-2\int_0^r \sigma(\lambda,r')dr'}\epsilon(\lambda)\epsilon(r), \tag{2}$$

which describes the amount of light received from an arbitrary range r. Combining all of the instrument specific constants into a single calibration constant C_λ, eqn(2) can be re-written as [5]

$$P_\lambda(r) = \frac{P_{t,\lambda}C_\lambda\beta(\lambda,r)T^2(\lambda,r)}{r^2}, \tag{3}$$

where

$$T^2(\lambda,r) = e^{-2\int_0^r \sigma(\lambda,r')dr'}, \tag{4}$$

is the total atmospheric transmission. Note that the overlap function $\epsilon(r) = 1$ is used because the lidar inversion is performed over ranges where the overlap function is nearly equal to one.

The two component model of the atmosphere takes into account Mie scattering from atmospheric aerosols and Rayleigh scattering from atmospheric molecules. As described by Wang et al. [8], the backscatter coefficient can be written in terms of these atmospheric scattering components as

$$\beta(\lambda,r) = \beta_A(\lambda,r) + \beta_R(\lambda,r), \tag{5}$$

where $\beta_A(\lambda, r)$ is the backscatter coefficient associated with the atmospheric aerosols and $\beta_R(\lambda, r)$ is the backscatter coefficient associated with the atmospheric molecules. Similarly, the extinction coefficient can be written as [8]

$$\sigma(\lambda, r) = \sigma_A(\lambda, r) + \sigma_R(\lambda, r), \tag{6}$$

where $\sigma_A(\lambda, r)$ is the extinction coefficient associated with the atmospheric aerosols and $\sigma_R(\lambda, r)$ is the extinction coefficient associated with the atmospheric molecules. The lidar inversion technique assumes that both the lidar ratio associated with the atmospheric aerosols, $S_A(\lambda) = \frac{\sigma_A(\lambda,r)}{\beta_A(\lambda,r)}$, and the lidar ratio associated with the atmospheric molecules, $S_R(\lambda) = \frac{\sigma_R(\lambda,r)}{\beta_R(\lambda,r)}$, are constant with respect to altitude. The assumption of the constant lidar ratio allows the total atmospheric transmission to be written as [8]

$$T^2(\lambda, r) = T_A^2(\lambda, r) T_R^2(\lambda, r), \tag{7}$$

where

$$T_A^2(\lambda, r) = exp[-2S_A(\lambda) \int_0^r \beta_A(\lambda, r')dr'] \tag{8}$$

is the atmospheric transmission due to atmospheric aerosols and

$$T_R^2(\lambda, r) = exp[-2S_R(\lambda) \int_0^r \beta_R(\lambda, r')dr'] \tag{9}$$

is the atmospheric transmission due to atmospheric molecules.

The assumption of a two component atmosphere requires altitude resolved knowledge of the molecular extinction and backscatter coefficients. Models of these coefficients are accurate enough for use in the inversion of lidar data. The temperature as a function of altitude h for 0 to 11 km can be modeled as [5]

$$T(h) = 288.15 - 0.00654h \tag{10}$$

where h is the height above mean sea level given in meters and the temperature, $T(h)$, is given in Kelvin. The pressure over the same altitude range can be modeled as [5]

$$P(h) = 1.013 \times 10^5 \left[\frac{288.15}{T(h)}\right]^{-5.2199} \tag{11}$$

where the pressure, $P(h)$, is given in Pascals. The molecular backscatter coefficient can be computed from the temperature and pressure profiles using the following equation [5]

$$\beta_R(\lambda, r) = \frac{374.28\left(\frac{P(h)}{T(h)}\right)}{\lambda^4} \tag{12}$$

where λ is given in nm and $\beta_R(\lambda, r)$ is given in (meter steradians)$^{-1}$. The extinction coefficient can then be found using $S_R(\lambda) = \frac{8\pi}{3}$.

Inserting eqn(5) and eqn(7) into eqn(3),the lidar equation for a two component atmosphere can be written as

$$P_\lambda(r) = \frac{P_{t,\lambda} C_\lambda \left[\beta_A(\lambda, r) + \beta_R(\lambda, r)\right] T_A^2(\lambda, r) T_R^2(\lambda, r)}{r^2}. \tag{13}$$

The lidar inversion can then be completed by solving eqn(13) for the aerosol backscatter coefficient, $\beta_A(\lambda, r)$, using the techniques presented in [7], which are outlined below. Taking the derivative of eqn(8) with respect to r yields

$$\frac{dT_A^2(\lambda, r)}{dr} = -2S_A(\lambda)\beta_A(\lambda, r)T_A^2(\lambda, r). \tag{14}$$

Solving eqn(13) for $\beta_A(\lambda, r)$ and substituting into eqn(14) yields the first order differential equation

$$\frac{dT_A^2(\lambda, r)}{dr} - 2S_A(\lambda)\beta_A(\lambda, r)T_A^2(\lambda, r) = -\frac{2S_A(\lambda)r^2 P_\lambda(r)}{P_{t,\lambda} C_\lambda T_R^2(\lambda, r)}, \tag{15}$$

which can be solved for $T_A^2(\lambda, r)$:

$$T_A^2(\lambda, r) = e^{2S_A(\lambda)\int_0^r \beta_R(\lambda, r')dr'} \times \left[1 - \frac{2S_A(\lambda)}{C_\lambda}\int_0^r \frac{r'^2 P_\lambda(r')}{P_{t,\lambda} T_R^2(\lambda, r')} e^{2S_A(\lambda)\int_0^{r'} \beta_R(\lambda, r'')dr''} dr'\right]. \quad (16)$$

Substituting eqn(16) into eqn(13), and solving for $\beta_A(\lambda, r)$ yields

$$\beta_A(\lambda, r) = \frac{L_\lambda(r) e^{-2(S_A(\lambda) - S_R(\lambda))\int_0^r \beta_R(\lambda, r')dr'}}{C_\lambda P_{t,\lambda} - 2S_A(\lambda)\int_0^r \frac{L_\lambda(r')}{T_R^2(\lambda, r')} e^{-2S_A(\lambda)\int_0^{r'} \beta_R(\lambda, r'')dr''} dr'} - \beta_R(\lambda, r) \quad (17)$$

where the range corrected return signal is defined as

$$L_\lambda(r) = r^2 P_\lambda(r). \quad (18)$$

The outgoing laser pulse and the telescope field of view are not in full overlap at altitudes below approximately 0.5 km. Therefore the lidar inversion is computed starting at an initial altitude r_0 that is at or above the altitude at which the transmitter and receiver come into full overlap [7, 8]. This can be accounted for by modifying eq.(17) so that

$$\beta_A(\lambda, r) = \frac{L_\lambda(r) e^{-2(S_A(\lambda) - S_R(\lambda))\int_{r_0}^r \beta_R(\lambda, r')dr'}}{C_\lambda P_{t,\lambda} T^2(r_0) - 2S_A(\lambda)\int_{r_0}^r \frac{L_\lambda(r')}{T_R^2(\lambda, r')} e^{-2S_A(\lambda)\int_{r_0}^{r'} \beta_R(\lambda, r'')dr''} dr'} - \beta_R(\lambda, r) \quad (19)$$

Table 3: Aerosol parameters derived from AERONET study [9].

Aerosol Species	$S_{A,550}$ (S.D.)*	$S_{A,550}/S_{A,1020}$ (S.D.)*	$\beta_{A,550}/\beta_{A,1020}$ (S.D.)*	$\sigma_{A,550}/\sigma_{A,1020}$ (S.D.)*
Biomass Burning	60 (8)	2.1 (0.3)	1.8 (0.3)	3.8 (0.4)
SE Asia	58 (10)	1.5 (0.3)	1.6 (0.2)	2.4 (0.3)
Urban/Industrial	71 (10)	1.9 (0.3)	1.6 (0.2)	3.3 (0.5)
Oceanic	28 (5)	1.0 (0.2)	1.4 (0.1)	1.5 (0.4)
Dust	42 (4)	1.2 (0.1)	0.9 (0.1)	1.2 (0.1)

*S.D. = standard deviation (Gaussian Dist.)

where the initial laser pulse energy, $P_{t,\lambda}$, has been scaled by the transmission of the atmosphere between the ranges $r = 0$ and $r = r_0$, $T^2(\lambda, r_0)$ [8].

The lidar inversion technique described above requires the assumption of a constant aerosol lidar ratio, $S_A(\lambda)$. Cattrall et al. [9] measured the aerosol lidar ratio for a variety of key aerosol species using ground-based retrievals of aerosol properties from selected AERONET sites around the world. Through careful selection of the AERONET sites and time of the observations, Cattrall et al. [9] were able to study the lidar ratio at 550 nm and 1020 nm when single aerosol species were dominant. Through these observations, the lidar ratios were studied for key aerosol types including Biomass Burning, South East Asia, Urban Industrial, Oceanic, and Dust. The results of this study of the lidar ratio of these key aerosol types have led to the Constrained Ratio Aerosol Model (CRAM), which is summarized in Table 3. The second column of Table 3 lists the lidar ratio and standard deviation at 550 nm for the various aerosol types while the third column lists the ratio and standard deviation of the aerosol lidar ratio at 550 nm to the aerosol lidar ratio at 1020 nm for the various aerosol types. The fourth and fifth columns list the extinction ratios, $\frac{\sigma_{550}}{\sigma_{1020}}$, and backscatter ratios, $\frac{\beta_{550}}{\beta_{1020}}$, respectively.

The CRAM model allows one to choose an initial lidar ratio, $S_A(\lambda)$, for the 532 nm and 1064 nm wavelengths, which are assumed to be the same as the lidar ratios at

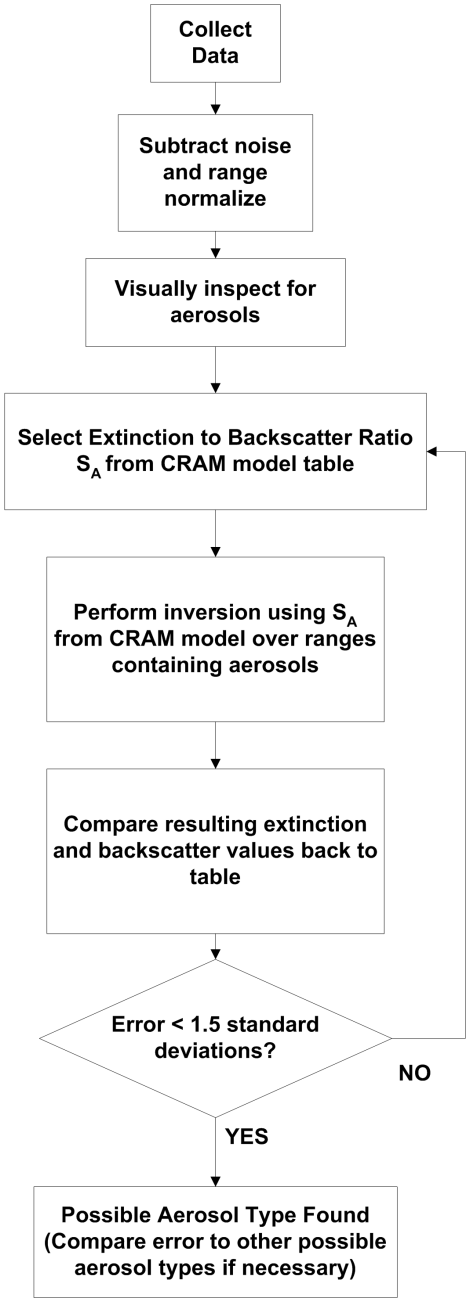

Figure 14: A flow diagram of the data processing algorithm, which is carried out using Matlab (tm) software.

550 nm and 1020 nm respectively. Using the lidar ratios, $S_A(\lambda)$ and $S_R(\lambda)$, from the CRAM model and the Rayleigh scattering model described above in eq.(10-12), the aerosol backscatter coefficients, $\beta_A(\lambda)$, at 532 nm and 1064 nm can be calculated using eq.(19) for the various aerosol species. The aerosol extinction coefficients, $\sigma_A(\lambda)$, are then calculated from backscatter coefficients using the same modeled lidar ratios. The ratio of the backscatter coefficient at 532 nm to the backscatter coefficient at 1064 nm $\frac{\beta_{532}}{\beta_{1064}}$ and the ratio of the extinction coefficient at 532 nm to the extinction coefficient at 1064 nm $\frac{\sigma_{532}}{\sigma_{1064}}$ are then calculated based on the results of the lidar inversion. If these ratios fall outside of 1.5 standard deviations from the values listed in table 3, the initial assumption regarding the aerosol species is deemed not valid. If the ratios fall within 1.5 standard deviations, the initial assumption is deemed valid. The valid aerosol species that produces the smallest deviation away from the model values of the aerosol backscatter ratio and aerosol extinction ratio listed in table 3 is chosen as the prevalent aerosol species. A flow diagram of this process is shown in figure 14. The full Matlab (tm) data processing code is included in appendix B.

Instrument Calibration

Calibration of the lidar instrument is necessary to ensure that an inversion performed on the lidar return data accurately identifies aerosol species recorded in those data. The 532 nm channel of the lidar is calibrated using data collected from above the boundary layer where molecular scattering dominates the return signal. Plugging eq.(13) into eq.(18) results in [10]

$$L_{532}(r) = P_{t,532}\beta_R(532, r)C_{532}T^2(532, r) \tag{20}$$

where the calibration constant, C_{532}, is calculated by inserting the modeled $T_R^2(532, r)$ and $\beta_R(532, r)$ values from eqs(9,12) and $T_A^2(532, r)$ which has been independently measured (possibly using a solar radiometer).

There is not enough molecular backscatter at 1064 nm to directly calibrate the 1064 nm channel of the lidar. The calibration of the 532 nm channel is transferred to the 1064 nm channel using optical depth measurements of a cirrus cloud at each wavelength. The round trip transmittance of the cloud, $T_{c,\lambda}^2$, is calculated by taking the ratio of the normalized lidar return, $X_\lambda(r) = \frac{L_\lambda(r)}{P_{t,\lambda}}$, above and below the cloud [10]

$$T_{c,\lambda}^2 = e^{-2\sigma_{c,\lambda}(r)} = \frac{X_\lambda(r_{ct})}{X_\lambda(r_{cb})} \tag{21}$$

where $\sigma_{c,\lambda}$ is the total extinction of the cloud, r_{ct} is the range of the top of the cloud and r_{cb} is the range of the bottom of the cloud. The cloud transmittance from eq.(21) can be inserted into

$$C_{1064} = \frac{C_{532} T(1064, r_{cb}) T_{c,532}^2 \int_{r_{cb}}^{r_{ct}} X_{1064}(r) dr}{T(532, r_{cb}) T_{c,1064}^2 \int_{r_{cb}}^{r_{ct}} X_{532}(r) dr} \tag{22}$$

to calculate the 1064 nm calibration constant C_{1064} based on the 532 nm calibration constant and the cirrus cloud measurements.

PROCEDURE

One Time Tasks

A few of the procedures required to get useful data from the two-wavelength lidar instrument only need to be done once. These tasks include characterization of the optics and detectors, system calibration and alignment of the laser with the telescope field of view. The characterization of optics and detectors has been covered thoroughly in Chapter 2. System calibration has been carried out very similarly to the procedure outlined in Chapter 3, with some simplification to reduce the complexity of the computation. A data set was found that met the criteria for calibration (i.e. a cirrus cloud with clean air immediately below), and also appeared to have essentially no aerosol present. Using this data set, the assumption was made that the atmospheric aerosol transmission term could be dropped out of eqn(20), resulting in

$$L_{532}(r) = P_{t,532}\beta_R(532, r)C_{532}T_R^2(532, r). \tag{23}$$

This allows the instrument to be calibrated without making independent measurements of the atmospheric aerosol transmission while collecting the calibration data set.

The procedure for aligning the laser with the telescope field of view is straight forward. First, the overlap is peaked up at low altitudes by maximizing the lidar return at those low altitudes. The lidar instrument is then aimed at a high cloud preferably at least 8 or 9 km in altitude so that the signal can be peaked up at this higher altitude. This ensures full overlap at high altitudes.

Frequent Tasks

Once the lidar data has been recorded by the computer, it is range corrected and energy normalized, then visually inspected to find possible aerosol regions. After this, an inversion is performed on the region of suspected aerosol. To this end, the computer inversion algorithm plugs lidar ratios $S_A(532)$ and $S_A(1064)$ for 532 nm and 1064 nm into eqn(19) from table 3 one at a time. The other terms in eqn(19) consist of the lidar return data $L_\lambda(r)$, known lidar instrument parameters C_λ and $P_{t,\lambda}$ and molecular scattering terms $\beta_R(\lambda, r)$ and $T_R^2(\lambda, r)$ that are modeled using eqn(9)-eqn(12). As described in Chapter 3, the resulting aerosol backscatter values, $\beta_A(\lambda, r)$, and corresponding extinction values, $\sigma_A(\lambda, r)$, that have been calculated using the relationship $S_A(\lambda) = \frac{\sigma_A(\lambda,r)}{\beta_A(\lambda,r)}$ are compared to their corresponding values in table 3. Specifically the ratio of the 532 nm backscatter coefficient divided by the 1064 nm backscatter coefficient is compared to the corresponding value in the 4^{th} row and the ratio of the 532 nm extinction coefficient divided by the 1064 nm extinction coefficient is compared to the corresponding value in the 5^{th} row. If an aerosol model produces new backscatter and extinction ratios that are within 1.5 standard deviations of the modeled values, that aerosol type is taken to be the prevalent type in the lidar data. If multiple aerosol types fall into this category, than the one that produces backscatter and extinction ratios that are the smallest number of standard deviations from the mean value is taken to be the prevalent aerosol type. This is done rather than using an un-weighted distance from the mean value because some of the modeled aerosol parameters have significantly larger standard deviations than others. Once the dominant aerosol species in a lidar return is known, extinction to backscatter ratios from table 3 are plugged in to eqn(19) along with modeled molecular backscatter and extinction data and measured lidar instrument constants to calculate a range resolved

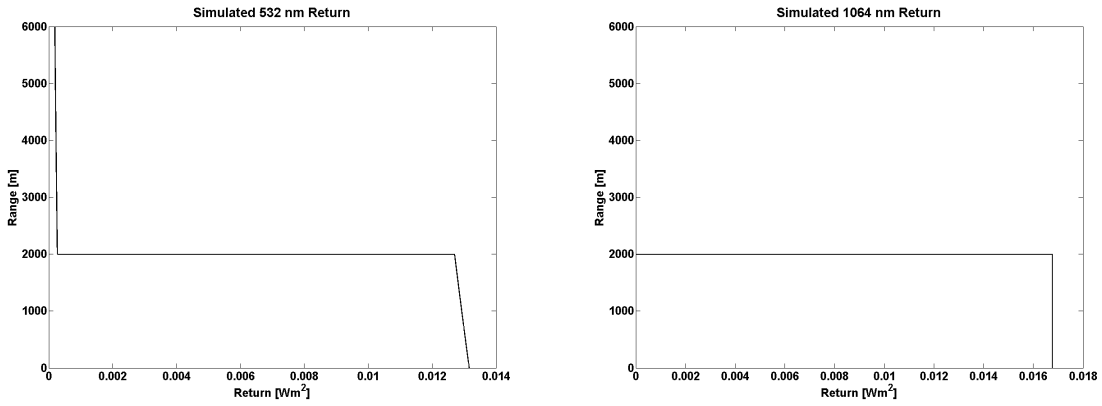

Figure 15: Simulated range and energy normalized lidar data containing Oceanic type aerosols. Aerosols are present in this data-set between 0 and 2000 km.

backscatter coefficient profile.

Example

The following is an example of the procedure outlined previously using simulated lidar return data. Simulated range and energy normalized lidar returns are shown in Figure 15. Since these data have already been range and energy normalized, they are then inspected to locate regions of aerosol. An aerosol plume is present in these data in ranges 1-2000 m, so the inversion will be calculated over this range. This part of the lidar return is inserted into eqn(19) along with the extinction to backscatter ratios presented in columns 2 and 3 of Table 3 to calculate the backscatter coefficient for each wavelength(each row is inserted one at a time with a separate backscatter coefficient being calculated for each row in the table). Extinction is then calculated for each row in the table based on the backscatter coefficient and the extinction to backscatter ratio from the table (again for each row). A ratio is then computed consisting of the 532 nm extinction and backscatter coefficients divided by the corresponding 1064 nm values. The difference between these values and the corresponding ratios contained in columns 4 and 5 of the CRAM table are computed. These differences are displayed

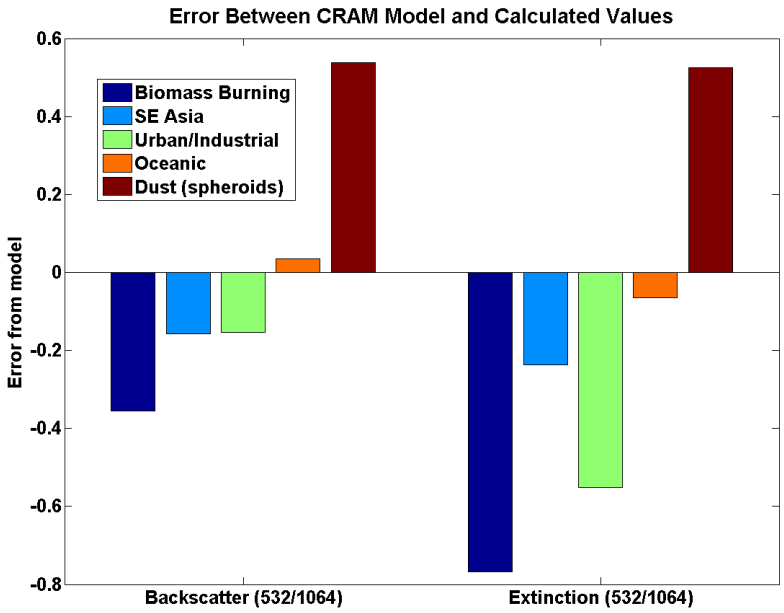

Figure 16: A plot of the error between expected lidar parameters for Oceanic aerosol contained in the CRAM lookup-table and those calculated using modeled Oceanic aerosol extinction to backscatter ratios taken from the same lookup-table.

in Figure 16. Note that the new extinction and backscatter ratios for the Oceanic model are within 1.5 standard deviations of the corresponding values in the CRAM table. The dominant aerosol species present in the simulated lidar data is therefor taken to be Oceanic. Finally, range resolved backscatter plots are created by inserting the simulated lidar data and the Oceanic extinction to backscatter ratios from the CRAM table are calculated (see Figure 17).

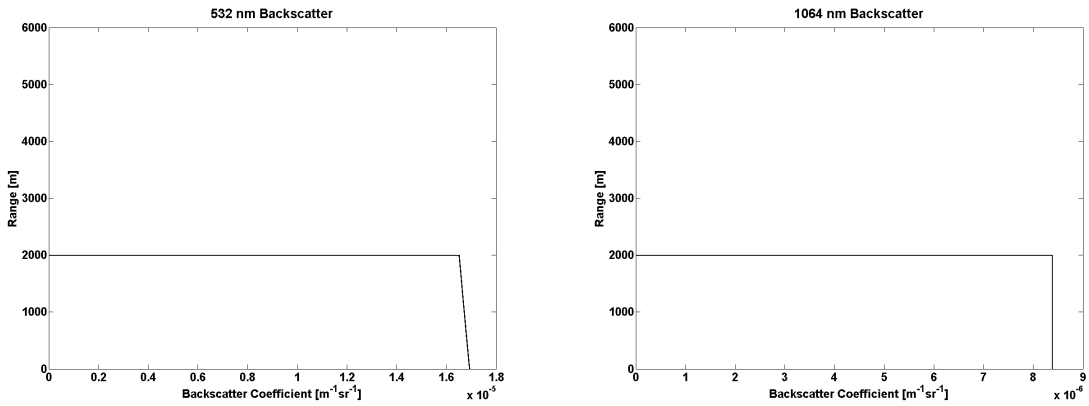

Figure 17: Range resolved backscatter plots computed using the simulated lidar data shown in Figure 15 as well as the Oceanic aerosol parameters from the CRAM lookup-table.

RESULTS

In this section, results from the two-wavelength lidar instrument are presented. These results consist of range-normalized lidar returns, aerosol species identification based on model-error, and range resolved backscatter plots for 1064 nm and 532 nm. Additionally, the algorithms designed for the two-wavelength instrument were applied to CALIPSO satellite data for varification purposes.

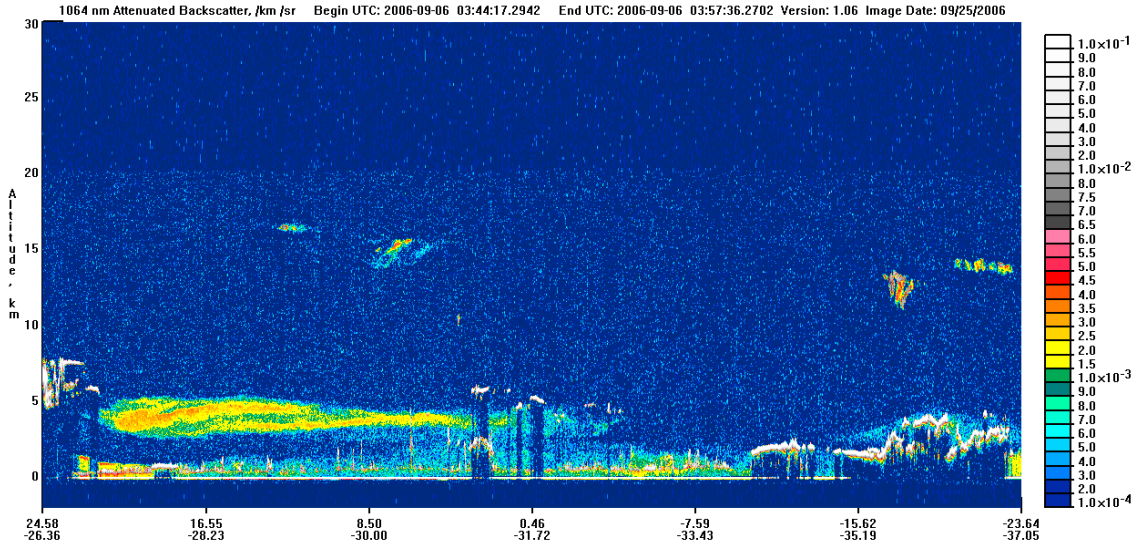

Figure 18: Data collected from the CALIOP lidar instrument on the CALIPSO satellite showing an elevated plume of Saharan dust off the coast of Africa [11].

CALIOP Data Results

To verify that the inversion algorithm developed for the two-color lidar is working properly, it was first tested using data from the CALIOP lidar on board the CALIPSO satellite. Data obtained from the NASA Langley Research Center Atmospheric Science Data Center [11] containing an elevated plume of Saharan dust is shown

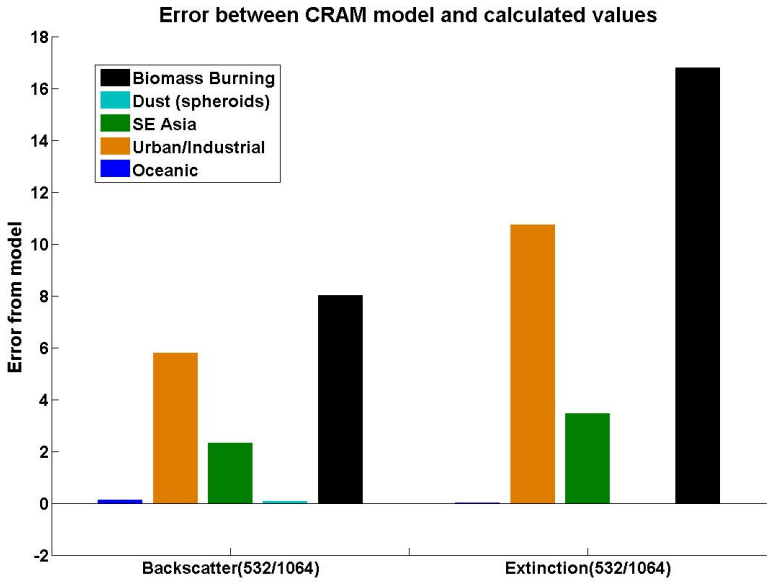

Figure 19: A plot of the error between expected lidar parameters and those calculated using modeled extinction to backscatter ratios according to the CRAM approach.

in figure 18. When the lidar inversion based on the CRAM model was applied to the data in figure 18, the aerosol species that produced the most self consistent results was the dust model. This means the ratios of extinction and backscatter, $\sigma_{532}/\sigma_{1064}$ and β_{532}/β_{1064}, resulting from an inversion computed using lidar ratios S_{550} and S_{1020} from the "Dust" row in table 3 were within 1.5 standard deviations of their corresponding values in the table. Plots of the errors between the calculated and modeled lidar parameters are shown in figures 19 and 20. These figures show the same data, but figure 20 has a smaller vertical scale to show small differences in errors between some of the models. Note that while the sum of squared errors is used to decide which model is a better fit, the errors plotted are raw error numbers (not squared). This has been done in an effort not to degrade the ammount of information containted in the plots. A range resolved plot of aerosol backscatter resulting from the inversion is shown in figure 21.

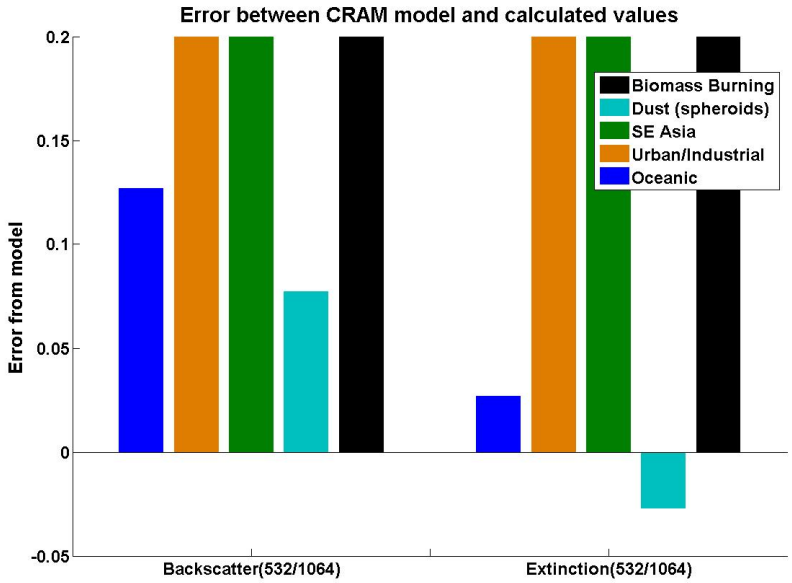

Figure 20: This plot is a zoomed in view of the plot in figure 19. It can be seen that the dust model produces the least error, leading to the conclusion that the aerosol plume in figure 18 is made up of dust.

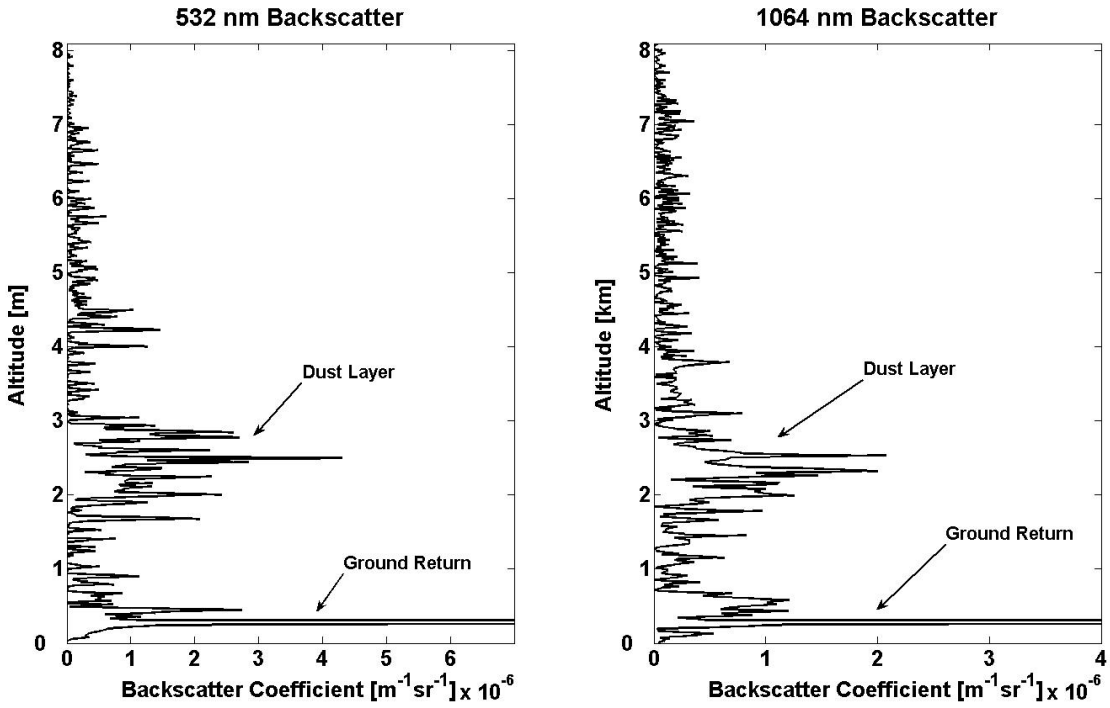

Figure 21: A plot of the 532 nm and 1064 nm range-resolved backscatter coefficients calculated from the lidar data presented in figure 18 using eqn(19) and the extinction to backscatter ratios from the dust model.

Ground Based Data Results

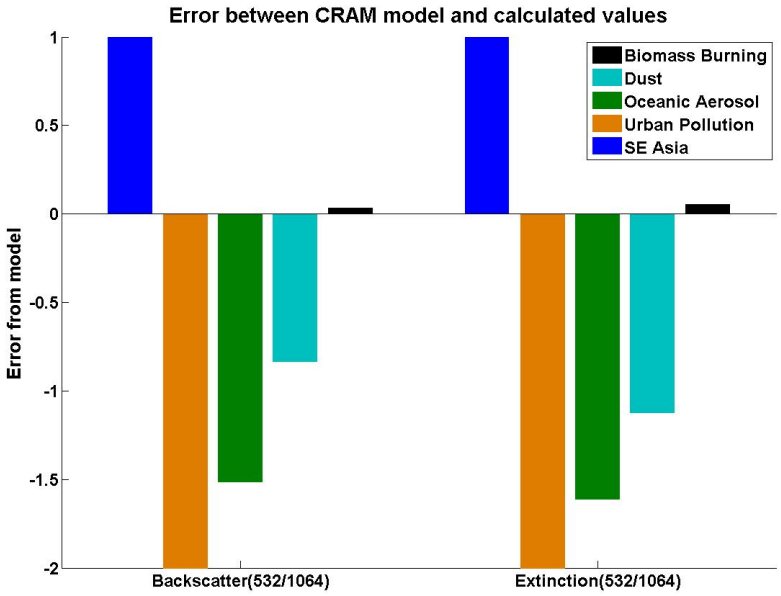

Figure 22: A plot of the error between expected lidar parameters and those calculated using modeled extinction to backscatter ratios according to the CRAM approach for the forest-fire data shown in figure 13. This error plot shows that biomass burning is the best model for the aerosol present in the data because this model produced by far the least error.

Data collected using the two color lidar, shown in figure 13, were taken during the fire season with a nearby forest fire burning. The range corrected data shown in these figures contain an elevated smoke plume extending horizontally across the image at approximately 3 km. Using the CRAM model the lidar inversion was computed for these data. As can be seen in figure 22, the biomass burning model is the best fit. The other models all resulted in significantly more error. This is the expected result, considering the forest fire smoke (a Biomass Burning type aerosol) present in the air during data collection. The range resolved backscatter coefficients for the 532 nm and 1064 nm channels of the two color lidar are shown in figure 23 based on the lidar

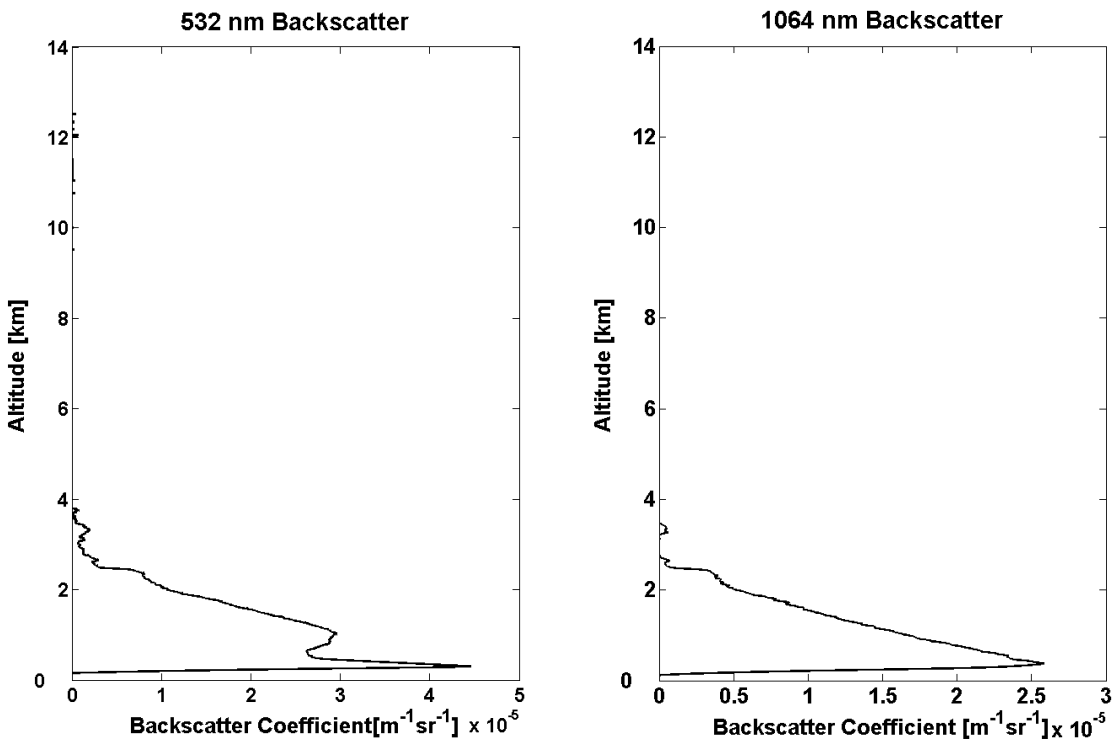

Figure 23: A plot of the 532 nm and 1064 nm range-resolved backscatter coefficients calculated from the lidar data presented in figure 13 using the extinction to backscatter ratios from the Biomass Burning model.

ratio associated with the Biomass Burning model. It should be noted that the two color lidar instrument does not come into full overlap until about 500 m.

Data collected during a winter temperature inversion event are presented in figure 24, showing an aerosol layer trapped near the ground. The CRAM inversion algorithm resulted in a finding of predominantly Urban/Industrial aerosols in the data. This is illustrated in figure 25 where the Urban/Industrial aerosol model clearly produced the least error. This appears to be a reasonable result, considering that all of the pollution in and around Bozeman (likely mainly from cars and industrial sources) was trapped near the ground by the temperature inversion, creating a stronger than usual plume of Urban/Industrial type aerosols. Figure 26 shows the range resolved

backscatter coefficients for this data.

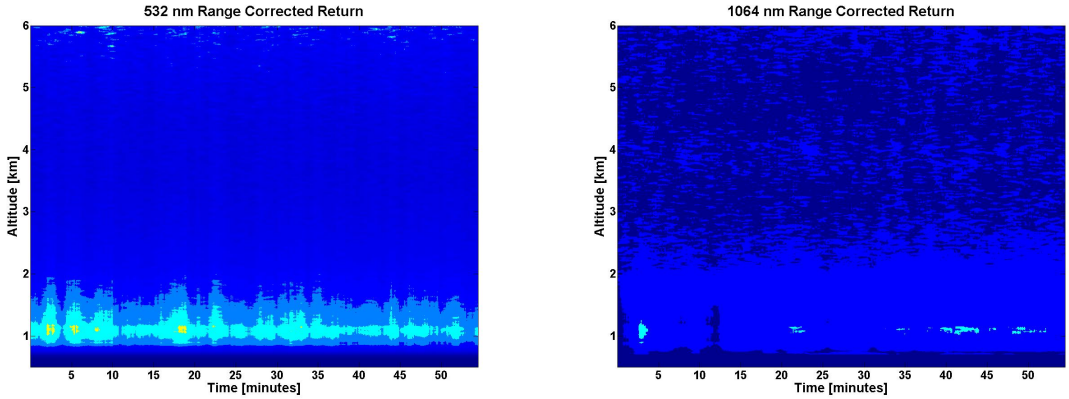

Figure 24: A plot of 532 nm and 1064 nm data collected during a winter temperature inversion event. An aerosol plume can be seen near the ground at approximately 1.2 km.

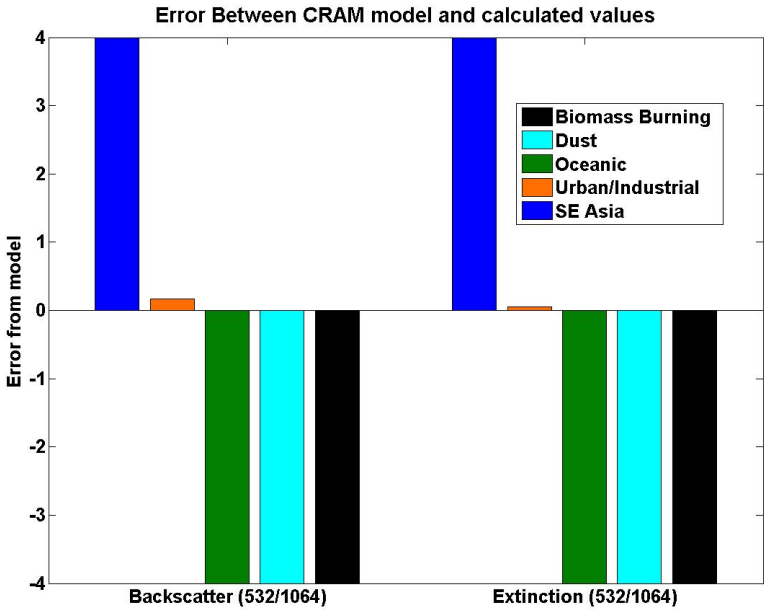

Figure 25: A plot of the error between expected lidar parameters and those calculated using modeled extinction to backscatter ratios according to the CRAM approach for the winter-inversion data shown in figure 24. This error plot shows that Urban/Industrial is the best model for the aerosol present in the data because this model produced the least error.

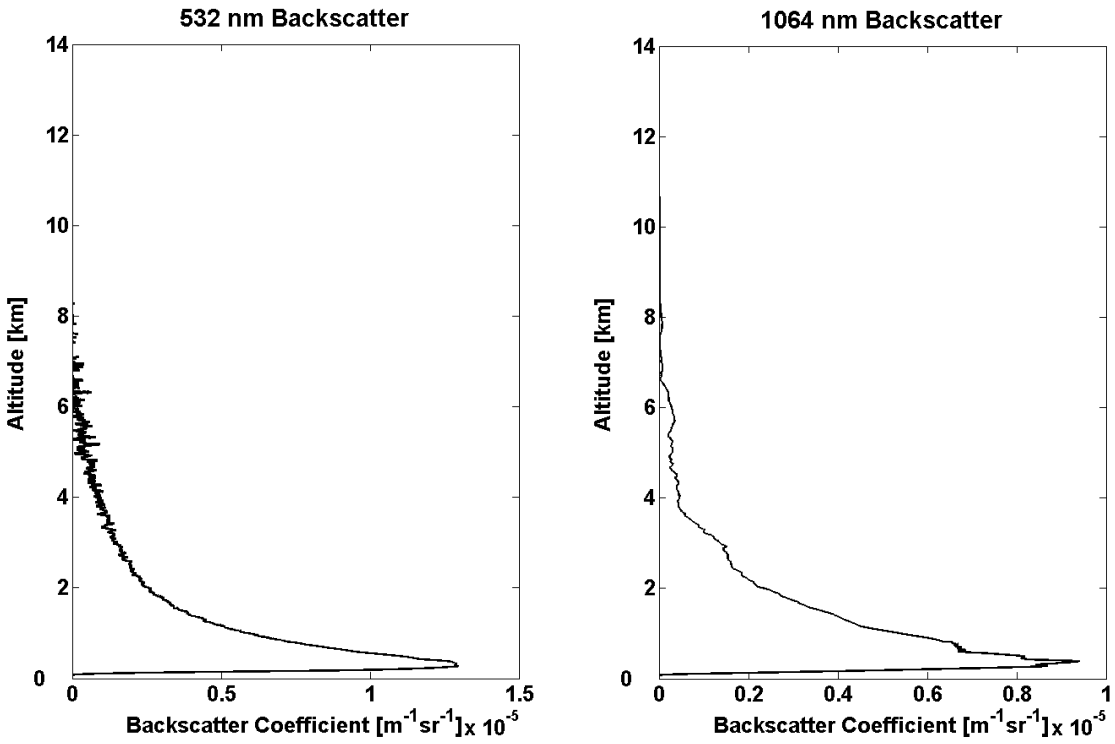

Figure 26: A plot of the 532 nm and 1064 nm range-resolved backscatter coefficients calculated from the lidar data presented in figure 24 using equation 19 and the extinction to backscatter ratios from the urban/industrial model.

ERROR ANALYSIS

Detector Signal to Noise Calculations

An important measure of the error present in the lidar return signal acquired by the two wavelength lidar instrument is the signal to noise ratio, which for the 532 nm channel of the lidar instrument can be expressed as [12]

$$SNR(r) = \frac{I(r)}{\sqrt{4eBG\left(\frac{1}{1-\frac{1}{\delta}}\right)I(r) + 4eBI_{dark} + \frac{4kTB}{R_L}}}, \tag{24}$$

where $I(r)$ is the photocurrent at the anode of the PMT generated by photons scattered from range r, e is the charge of an electron, B is the bandwidth of the PMT, G is the overall gain of the PMT, δ is the gain of an individual dynode stage of the PMT, I_{dark} is the dark current of the PMT (at the anode), k is Boltzmann's constant, T is the temperature in Kelvin and R_L is the load resistance. The photocurrent $I(r)$ can be expressed as a function of incident optical power as

$$I(r) = \frac{P(r)\lambda\nu Ge}{hc}, \tag{25}$$

where $P(r)$ is the optical power of light scattered by the atmosphere at range r (see eqn(2)), ν is the quantum efficiency of the PMT and h is Planck's constant. The signal to noise ratio is similar for the 1064 nm channel of the lidar instrument, and can be expressed as [13]

$$SNR(r) = \frac{I(r)G}{\sqrt{4eBG^2F(I(r) + I_{dark}) + 4eI_{dark,nogain} + \frac{4kTB}{R_L}}}, \tag{26}$$

where F is the excess noise factor, $I_{dark,nogain}$ is the dark current that is not multiplied by the gain and G is the gain of the APD. The photocurrent $I(R)$ can again be calculated using eqn(25).

Signal to noise measurements show how well the desired signal can be discerned from background noise. As the ratio of signal to noise approaches 1, the signal becomes difficult to distinguish from the noise. Range resolved plots of the signal to noise ratio for the two wavelength lidar instrument calculated using eqn(24-26) are shown in figures 27 and 28 for the 532 nm and 1064 nm channels of the lidar instrument, respectively. These signal to noise ratios were calculated using modeled atmospheric molecular backscatter profiles for each wavelength created using eqn(10-12). Other values used for the calculation include 80 mJ and 28 mJ for the 1064 nm and 532 nm laser pulse energies, 1 for the overlap function and 1.5 m for the range resolution. As is expected, the signal to noise ratio decays exponentially with range, and is improved by averaging multiple lidar returns together. Figures 29-31 and 32-34 contain 532 nm and 1064 nm data showing the effects of the signal to noise ratio on the range corrected lidar return signal, as well as the effects of averaging multiple returns together. The signal appears more degraded at longer ranges where the signal to noise ratio is worse. The signal becomes cleaner in appearance as more returns are averaged together.

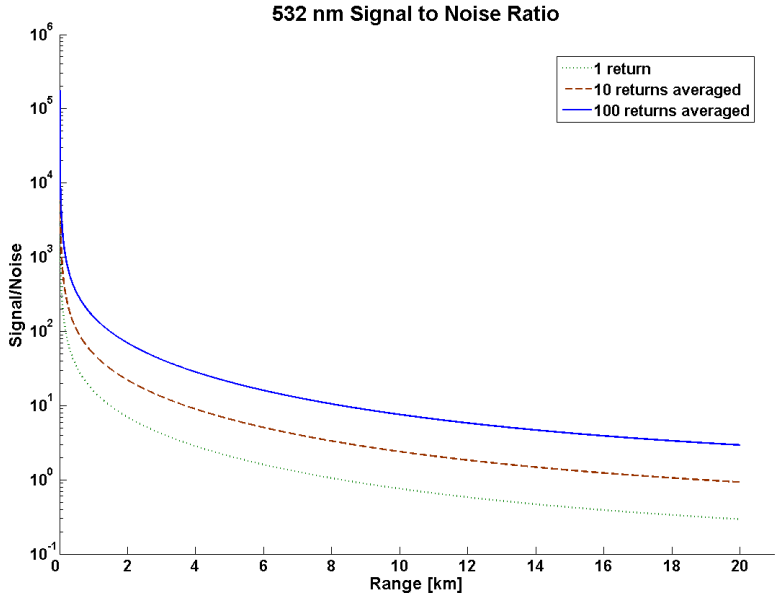

Figure 27: A plot of the signal to noise ratio for the 532 nm channel of the lidar instrument while averaging together 1, 10 and 100 lidar returns.

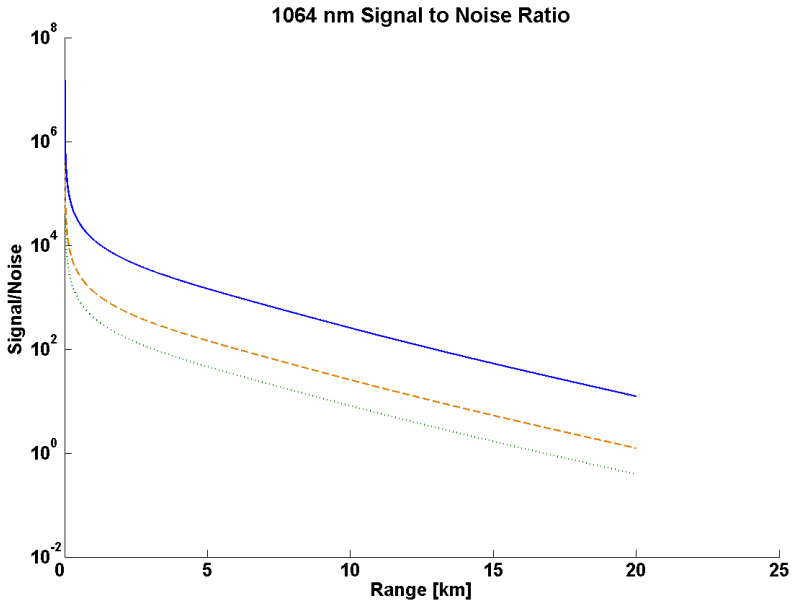

Figure 28: A plot of the signal to noise ratio for the 1064 nm channel of the lidar instrument while averaging together 1, 10 and 100 lidar returns.

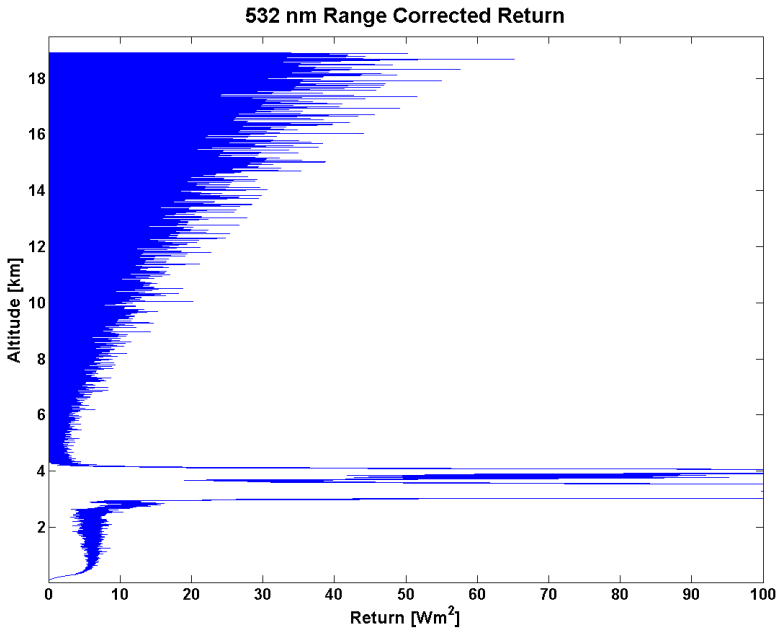

Figure 29: A 532 nm lidar return with no averaging.

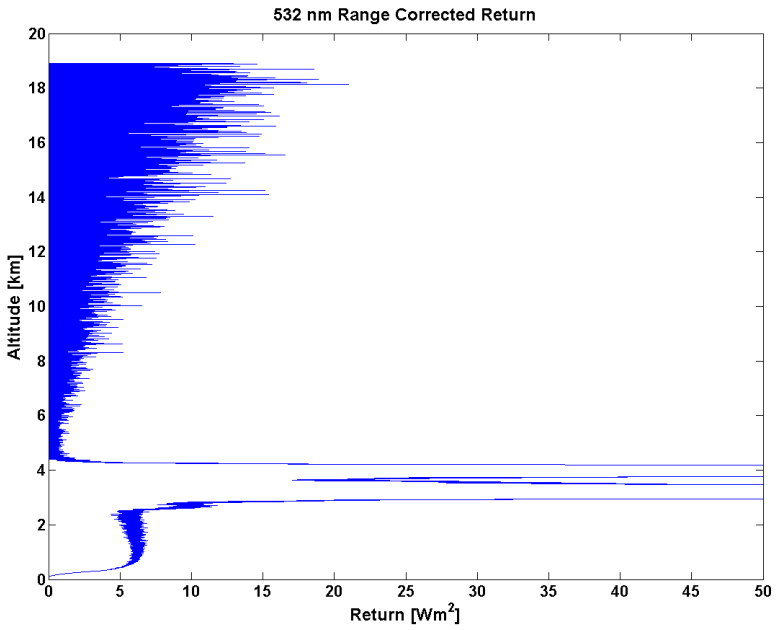

Figure 30: A 532 nm lidar return with 10-shot averaging.

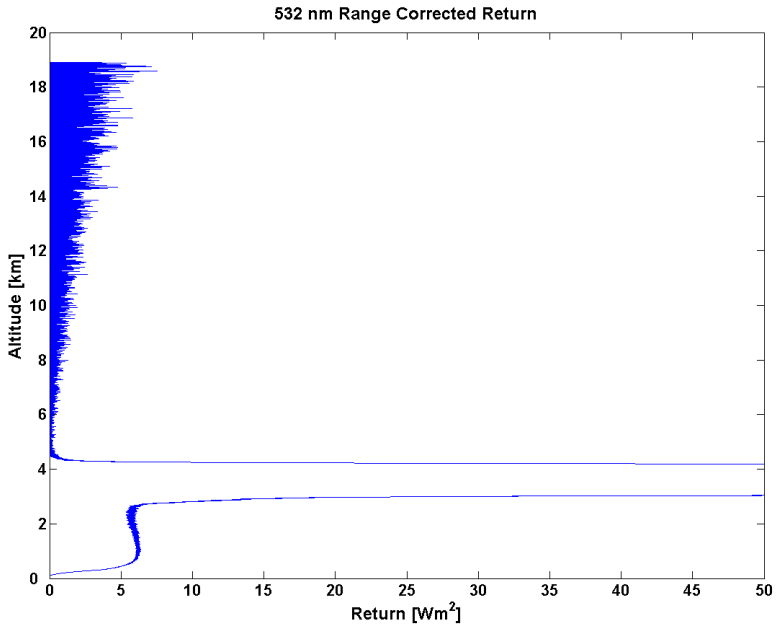

Figure 31: A 532 nm lidar return with 100-shot averaging

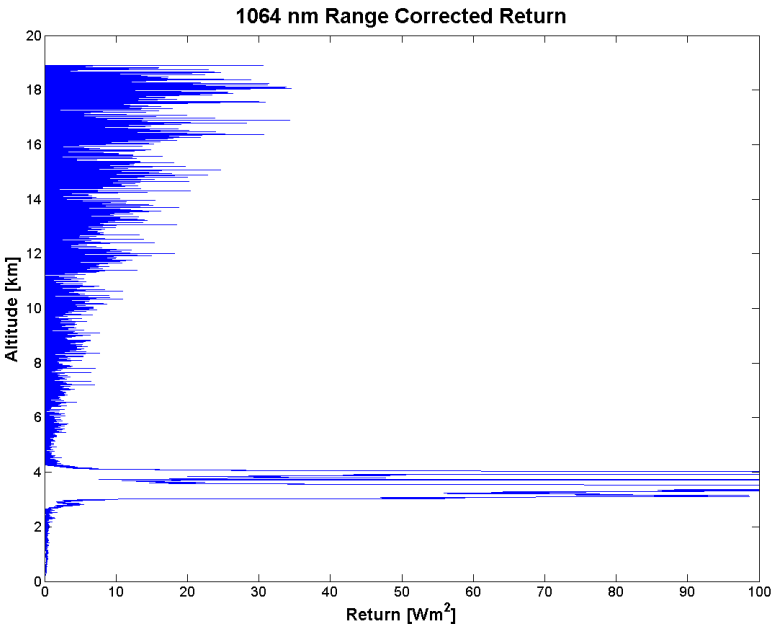

Figure 32: A 1064 nm lidar single shot return with no averaging

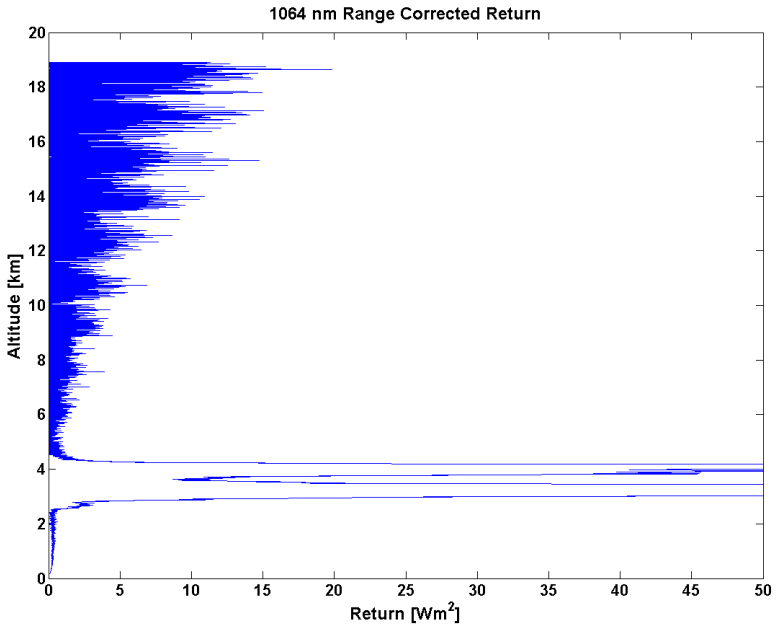

Figure 33: A 1064 nm lidar return with 10-shot averaging

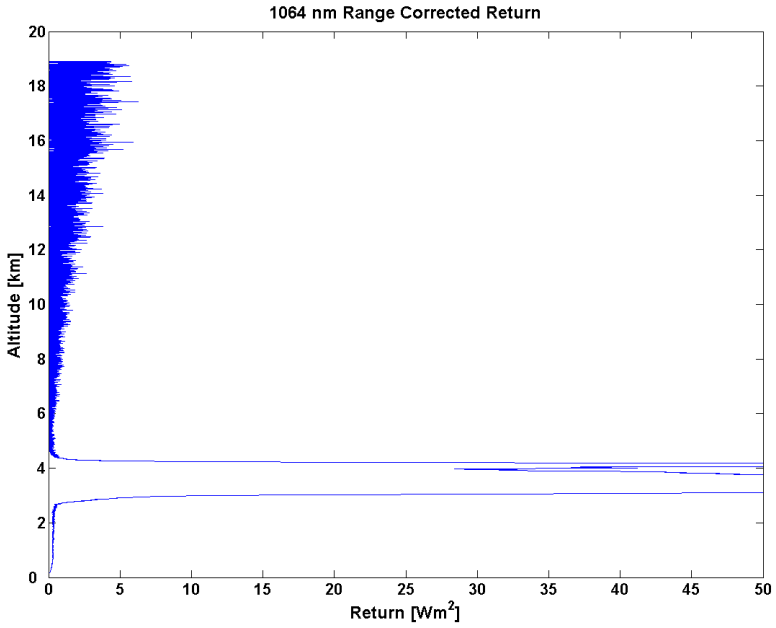

Figure 34: A 1064 nm lidar return with 100-shot averaging

Quantization Error

In addition to the noise added to the signal by the detectors themselves, quantization noise is added to both the 532 nm and the 1064 nm signals when they are digitized so that they can be stored and analyzed via computer. The digitization process consists of sampling the continuous voltage signal produced by the APD and the PMT at discrete time intervals, and rounding the voltage value of each sample to a discrete level that can be represented by the arbitrary number of bits used by the analog to digital (A/D) converter. The difference between the actual voltage value of the input signal from the lidar instrument and the discrete value assigned by the A/D card is the quantization noise (see figure 35). Because the signals from the APD and PMT in the two-wavelength lidar instrument are usually within the range of the A/D converter and the quantization levels of the A/D card are uniform, the quantization noise is essentially uniformly distributed random (white) noise. The quantization process can therefore be modeled (in terms of the signal to noise ratio of the overall system) as adding uniformly distributed random noise to each sample as shown in figure 36. The signal to noise ratio associated with the quantization process can be modeled as [14]

$$SNR_Q = \frac{12 \cdot 2^{2b}\sigma_x^2}{X_m^2}, \tag{27}$$

where SNR_Q is the signal to noise ratio resulting from the quantization process, $b+1$ is the number of bits used to represent the quantized data, σ_x^2 is the variance of the signal being quantized and X_m is the range of the quantizer input (the variance and the input range should use the same units; in the case of the two-wavelength lidar instrument the units are Volts). The signal to noise ratio associated with the quantization process is on the order of 10^{20}. This means that the noise introduced

by the digitization process is insignificant when compared to the noise introduced by the optical detectors.

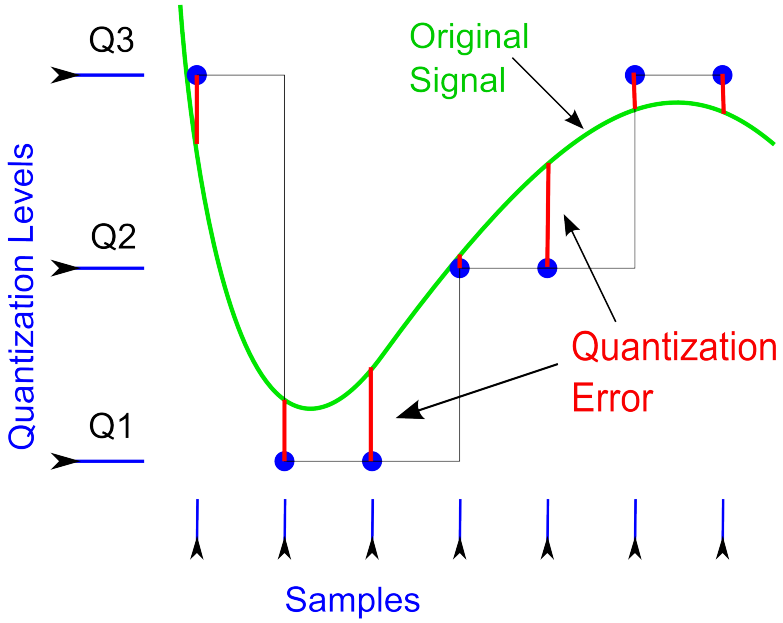

Figure 35: Quantization error is the difference between the actual signal and its quantized value; quantization occurs when the signal is digitized using an A/D converter. In this figure, the red vertical lines represent the quantization error, the blue horizontal lines along the left side mark the quantization levels and the blue vertical lines along the bottom mark the sample points where the original signal (the green line) is sampled and subsequently quantized.

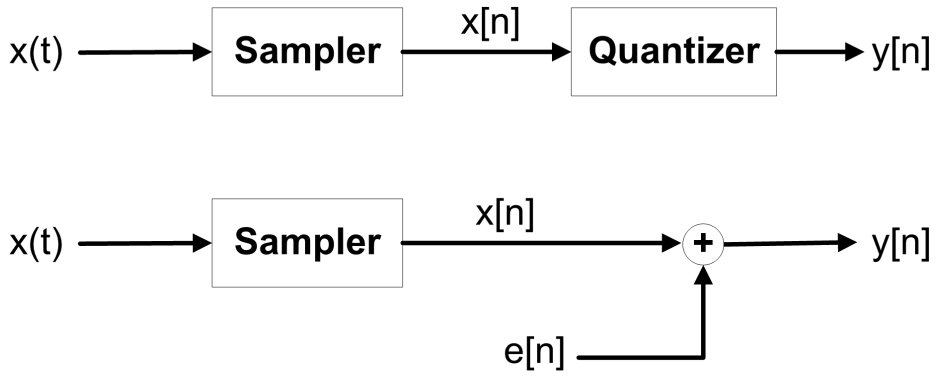

Figure 36: Quantization can be modeled as adding the error term $e[n]$ to the sampled signal, where $e[n]$ is uniformly distributed random noise.

Numerical Integration Error

The final source of error addressed in this thesis is caused by the use of numerical integration to approximate the continous integrals used to analyze data from the lidar instrument. Analysis of integration error was carried out empirically by varying the width of the sections being summed during the numerical integration process and observing changes in the results of the data analysis calculations. Specifically, this was accomplished by varying the sample rate of simulated lidar data. The true value of the data analysis calculations carried out on the simulated data were determined by increasing the sample rate until the calculation results converged. Numerical integration error was then determined as percent error from the true value of the calculation results as a function of sample rate, and is plotted in Figure 37. The numerical integration error for a sample rate of 200 MHz (the sample rate of the two-wavelength lidar intrument) was calculated to be approximately 0.34%. Considering that the standard deviations of many of the entries in the CRAM lookup-table used in the data analysis algorithm is on the order of $10-20\%$, this error does not significantly affect the outcome of the data analysis process.

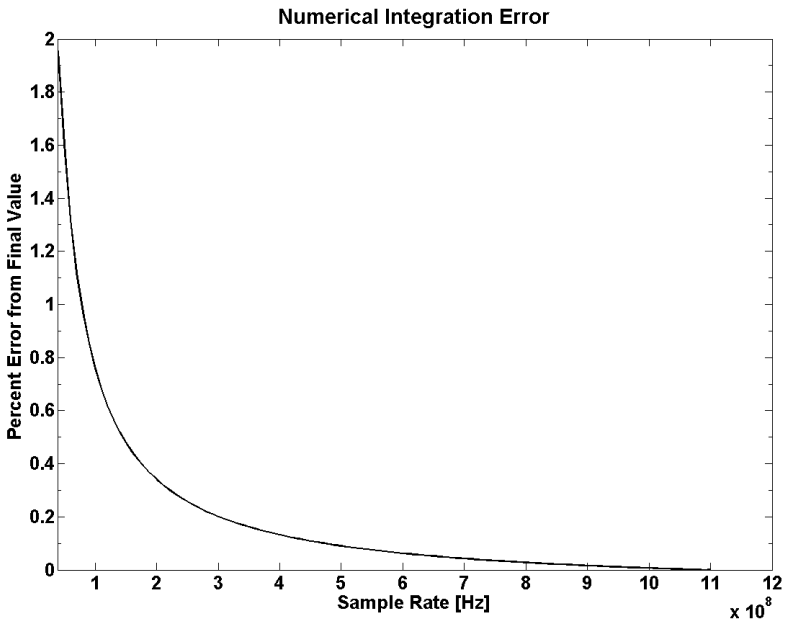

Figure 37: Percent error resulting from using numerical integration in the data analysis software. Note that at 200 MHz (the sample rate of the two-wavelength lidar instrument), the error is approximately 0.34%.

CONCLUSION

A two-color lidar has been developed at Montana State University for atmospheric aerosol studies. This instrument has been calibrated so that its data can be compared to data from other instruments such as the CALIOP lidar on board the CALIPSO satellite, and so that accurate inversions of the data can be performed. The inversion procedure has been verified using CALIOP satellite data with known aerosol content. This procedure results in identification of aerosol species present in the atmosphere as well as range resolved extinction and backscatter profiles. The capabilities of the ground based lidar system have been demonstrated by the successful inversion of its data.

Future Work

Due to the general uncertainty still surounding atmospheric aerosol radiative forcing of the earth's atmosphere, detailed studies of atmospheric aerosols are a major scientific priority. High spectral resolution lidar (HSRL) instruments show great promise because their data can be used to directly calculate aerosol extinction and backscatter profiles without requiring many of the assumptions needed to perform similar computations with two-wavelength lidar data.

An HSRL will be constructed at MSU in the near future for the purpose of aerosol study. This instrument will make separate measurements of molecular and aerosol scattering that can be used in conjunction with a modeled atmospheric molecular scattering profile to calculate extinction and backscatter as a function of altitude. To accomplish this, a narrowband pulsed laser is used to illuminate a portion the atmosphere and some of the scattered light is collected using a telescope. Light

scattered back from aerosols is similar spectrally to the narrowband light emitted from the laser, whereas light scattered by molecules has been spectrally broadened by a factor of approximately 100 due to the Doppler effect. The narrowband and broadened return will be separated via a confocal-cavity interferometer so that each part of the return can be recorded separately.

REFERENCES CITED

[1] P. Forster, V. Ramaswamy, P. Artaxo, T. Berntsen, R. Betts, D. Fahey, J. Haywood, J. Lean, D. Lowe, G. Mhhre, J. Nganga, R. Prinn, G. Raga, M. Schulz, and R. V. Dorland, "'changes in atmospheric constituents and in radiative forcing.' in: Climate change 2007: The physical science basis. contributions of working group i to the fourth assessment report of the intergovernmental panel on climate change [s. solomon and d. qin and m. manning and z. chen and m. marquis and k.b. averyt and m. tignor and and h.l. miller and eds.]," Cambridge University Press, Cambridge, United Kingdom and New York, NY, USA, 2007.

[2] R. Zhang, G. Li, J. Fan, D. L. Wu, and M. J. Molina, "Intensification of pacific storm track linked to asian pollution." *Proc Natl Acad Sci USA*, vol. 104, pp. 5295–5299, 2007.

[3] J. Penner, M. Andreae, H. Annegarn, L. Barrie, J. Feichter, D. Hegg, A. Jayaraman, R. Leaitch, D. Murphy, J. Nganga, and G. Pitari, "Aerosols, their direct and indirect effects, climate change 2001: The scientific basis. contribution of working group i to the third assessment report of the intergovernmental panel on climate change [houghton, j.t., y. ding, d.j. griggs, m. noguer, p.j. van der linden, x. dai, k. maskell, and c.a. johnson (eds.)]," Cambridge University Press, Cambridge, United Kingdom and New York, NY, USA, 2001.

[4] C. Eichel, M. Kramer, L. Shultz, and S. Wurzler, "The water soluble fraction of atmospheric aerosol particles and its influence on cloud microphysics," *J. Geophys. Res.*, vol. 101, no. 29, pp. 499–510, 1996.

[5] V. A. Kovalev and W. E. Eichinger, *Elastic Lidar: Theory, Practice and Analysis Methods*. John Wiley and Sons, New York, 2004, p. 444.

[6] D. S. Hoffman, A. R. Nehrir, K. S. Repasky, J. A. Shaw, , and J. L. Carlsten, "Range-resolved optical detection of honeybees by use of wing-beat modulation of scattered light for locating land mines," *Applied Optics*, vol. 46, no. 15, pp. 3007–3012, 2007.

[7] F. G. Fernald, B. M. Herman, and J. A. Reagan, "Determination of aerosol height distributions by lidar," *Journal of Applied meteorology*, vol. 77, pp. 433–448, 1989.

[8] X. Wang, J. Reagan, C. Cattrall, and K. Thome, "Spaceborne lidar aerosol retrieval approaches based on improved aerosol model constraints," in *IEEE Workshop on Remote Sensing of Atmospheric Aerosols, 2005*, April, 2005, pp. 36–42.

[9] C. Cattrall, J. Reagan, K. Thome, and O. Dubovik, "Variability of aerosol and spectral lidar and backscatter and extinction ratios of key aerosol types derived from selected aerosol robotic network locations," *J. Geophys. Res.*, vol. 110, 2005.

[10] J. A. Reagan, "Personal interview," 2007.

[11] *NASA Langley Research Center Atmospheric Science Data Center*. http://eosweb.larc.nasa.gov/, 2006.

[12] H. Corp., *High Speed Gated PMT Module H7680, H7680-01 Instruction Manual*. Hamamatsu Electron Tube Center, Japan, 2005.

[13] ——, *APD Module C5460SPL 6308 Instruction Manual*. Hamamatsu Solid State Division, Japan, 2007.

[14] A. V. Oppenheim, R. W. Shafer, and J. R. Buck, *Discrete Time Signal Processing*. Prentice Hall, Upper Saddle River, NJ, 1999, pp. 194–197.

APPENDICES

APPENDIX A

DETECTOR CHARACTERIZATION DATA

PMT Characterization Data

		PMT Response [V] for Gain Control Voltage:						
Reference Power [nW]	Incident Power [nW]	2 V	2.5 V	3 V	3.5 V	4 V	4.5 V	5 V
0.44	0.001527	0	0	0.002	0.006	0.026	0.094	0.14
0.57	0.001978	0	0	0.002	0.01	0.04	0.136	0.18
0.86	0.002984	0	0.0004	0.003	0.011	0.065	0.182	0.258
1.18	0.004094	0	0.0004	0.004	0.02	0.074	0.246	0.33
1.28	0.004441	0	0.0004	0.004	0.02	0.087	0.248	0.37
1.76	0.006107	0	0.0004	0.004	0.021	0.102	0.31	0.47
1.95	0.006766	0	0.0005	0.007	0.035	0.122	0.476	0.576
2.65	0.009195	0	0.0007	0.008	0.041	0.136	0.504	0.708
3.2	0.011103	0	0.0008	0.012	0.046	0.196	0.684	0.848
4	0.013879	0	0.0009	0.013	0.048	0.264	0.87	1.08
4.87	0.016898	0	0.001	0.015	0.066	0.292	1.02	1.26
5.12	0.017765	0	0.0013	0.015	0.071	0.292	1.13	1.42
6.98	0.024219	0	0.0014	0.025	0.08	0.416	1.56	1.89
10.63	0.036884	0	0.0016	0.033	0.16	0.68	2.06	2.68
13.87	0.048126	0	0.0025	0.042	0.204	0.872	2.44	3.5
16.02	0.055586	0	0.0027	0.047	0.192	1.03	3.26	4.1
20.82	0.072241	0	0.0036	0.063	0.236	1.45	4.22	5.22
26.62	0.092366	0.0005	0.0056	0.087	0.468	1.98	5.36	
35.5	0.123178	0.0006	0.008	0.107	0.518	2.66		
44.76	0.155308	0.0006	0.008	0.124	0.66	3.42		
54.59	0.189416	0.0007	0.011	0.146	0.88	4.14		
65.68	0.227896	0.0009	0.013	0.221	0.92	5.05		
77.6	0.269256	0.001	0.017	0.236	1.2			
89.91	0.31197	0.0012	0.019	0.287	1.4			
119.4	0.414294	0.0016	0.022	0.392	1.86			
137.8	0.478138	0.0016	0.027	0.426	2.15			
216.2	0.750171	0.0018	0.042	0.616	2.78			
271.5	0.942051	0.0022	0.045	0.81	3.34			
417.8	1.449682	0.003	0.054	1.03	4.96			
1183	4.104773	0.0035	0.065	1.28				
1813	6.290747	0.0043	0.069	1.42				
3992	13.85144	0.0066	0.098	1.8				
6081	21.09985	0.0077	0.108	2.14				

APD Characterization Data

Reference Power [νW]	Incident Power [νW]	APD Response [mV]
0.096	0.023301	2.62
0.137	0.033252	3.48
0.161	0.039078	4.04
0.189	0.045874	4.6
0.258	0.062621	5.84
0.367	0.089078	7.8
0.512	0.124272	10.9
0.682	0.165534	13.1
0.819	0.198786	15.4
0.96	0.23301	18.7
1.15	0.279126	22.3
1.57	0.381068	33
2.079	0.504612	41.2
2.927	0.710437	58.8
3.371	0.818204	66.4
4.727	1.14733	96.4
6.39	1.550971	126
8.24	2	156
8.399	2.038592	182
11.86	2.878641	241
16.26	3.946602	320
19.85	4.817961	386
22.85	5.546117	450
28.22	6.849515	572
33.06	8.024272	648
38.37	9.313107	708
46.54	11.29612	848

APPENDIX B

MATLAB CODE

Main Analysis Program

Main Analysis Program Driver

```
%This program starts the inversion process.  L_short2 and L_long2
%are range normalized lidar returns that need to be in the workspace
%to run this program


start = 900; %starting range bin for inversion
finish = 1025; % final range bin for inversion



error = look_up_sim(L_short2,L_long2,start,finish);  %calls error program

figure

bar(error') %plots error
```

LUT Function

```
function out = look_up_sim(L_short,L_long,start,finish)
%This function takes in two range normalized lidar returns L_short
%and L_long and returns a the error bettween the results
%calculated using each entry in the CRAM model table and the
%expected value



%here is the CRAM table:
table(:,:,1) = [60 8; 2.1 .3; 1.8 .3; 3.8 .4];  %biomass burning
table(:,:,2) = [58 10; 1.5 .3; 1.6 .2; 2.4 .3]; %SE Asia
table(:,:,3) = [71 10; 1.9 .3; 1.6 .2; 3.3 .5]; %Urban/Industrial
table(:,:,4) = [28 5; 1 .2; 1.4 .1; 1.5 .4];    %Oceanic
table(:,:,5) = [42 4; 1.2 .1; .9 .1; 1.2 .1];   %Dust
result = 7;
old_score = 200;
print = 0;
%test = 0;
score = 20;

%this computes extinction and backscatter and various
%ratios therof using extinction to backscatter numbers from the table
%for each aerosol type in the table.

for num = 1:5 %change this line to pick which types are tried
    S_short = table(1,1,num);
    S_long = S_short / table(2,1,num);
    k_exp = table(4,1,num)
    [alpha_S_new alpha_L_new backscatter_S_new backscatter_L_new] = multi_wav_lidar_sim(k_exp,
        L_short,L_long,S_short,S_long,start,finish); %calculate new lidar parameters
```

```
    alpha_S_new = mean(alpha_S_new(start:finish));
    alpha_L_new = mean(alpha_L_new(start:finish));
    backscatter_S_new = mean(backscatter_S_new(start:finish));
    backscatter_L_new = mean(backscatter_L_new(start:finish));
    error(num,:) = [((alpha_L_new/backscatter_L_new)-table(1,1,num)) (((alpha_L_new/
        backscatter_L_new)/(alpha_S_new/backscatter_S_new))-table(2,1,num)) ((backscatter_L_new/
        backscatter_S_new)-table(3,1,num)) ((alpha_L_new./alpha_S_new)-table(4,1,num))];
    if (((alpha_L_new/backscatter_L_new) <= (table(1,1,num)+table(1,2,num))) && ((alpha_L_new/
        backscatter_L_new) >= (table(1,1,num)-table(1,2,num))) && ((alpha_L_new/alpha_S_new) <= (
        table(4,1,num)+table(4,2,num))) && ((alpha_L_new/alpha_S_new) >= (table(4,1,num)-table
        (4,2,num)) ) && (((alpha_L_new/backscatter_L_new)/(alpha_S_new/backscatter_S_new)) <= (
        table(2,1,num)+table(2,2,num))) && (((alpha_L_new/backscatter_L_new)/(alpha_S_new/
        backscatter_S_new)) >= (table(2,1,num)-table(2,2,num))) )&& ((backscatter_L_new/
        backscatter_S_new) <= (table(3,1,num)+table(3,2,num))) && ((backscatter_L_new/
        backscatter_S_new) >= (table(3,1,num)-table(3,2,num)) )%find the model entry that produces
         the least error
       score = (((alpha_L_new/backscatter_L_new)-table(1,1,num))/table(1,2,num))^2 + (((
           alpha_L_new./alpha_S_new)-table(4,1,num))/table(4,2,num))^2 +((((alpha_L_new/
           backscatter_L_new)/(alpha_S_new/backscatter_S_new))-table(2,1,num))/table(2,2,num))^2 +
            (((backscatter_L_new/backscatter_S_new)-table(3,1,num))/table(3,2,num))^2
        if score < old_score
            old_score = score;

            result = num;
        end
    end
end



a_type = result

out = error;
```

Analysis Code

```
function [alpha_64, alpha_532, backscatter_64, backscatter_532] = multi_wav_lidar_sim(k_expected,
    L_short,L_long,S_short,S_long,start,finish)

%This function computes extinction and backscatter coefficients
%using lidar returns L_long and L_short and modeled extinction to
%backscatter ratios S_long and S_short from ranges 'start' to 'finish'


delr = (1/200000000)*((3*(10^8))/2); %size of a range bin

C = 523;

lth = size(L_short,2); %length of input lidar return
n = [start:1:lth];
h = (n/200000000)*((3*(10^8))/2); %build height array
T = 288.15 - (.006545.*h);  %Temperature profile
p = ((288.15./T).^(-.034164/.006545)).*(1.013e5); %pressure profile
```

```
wav = 532;
backscatter_M = (3742.8*(p./T)./(wav^4)); %molecular backscatter

alpha_M = ((backscatter_M .*(8*pi))./3); %molecular extinction

S_M = (8*pi)/3; %molecular extinction to backscatter ratio

%TL = .73;

T2 = alt;  %molecular transmission is calculated here:
for n = 1:lth
    T2(n) = exp(-2*sum(alpha_M(1:n)))./(n^2);
end
TL = T2;
k = k_expected;


%Computation of aerosol backscatter, then extinction using lidar eqn:
int_funct = zeros(1,finish);
for n = start:finish
    int_funct(n) = sum(backscatter_M(n-start+1:finish-start+1))*delr;
end

backscatter_532 = zeros(1,finish);
for n = start:finish
    backscatter_532(n) = (L_short(n)*exp(2*(S_short-S_M)*(sum(backscatter_M(n-start+1:finish-start
        +1))*delr)))/((C*(TL(n)^2))-(2*S_short*(sum(L_short(n:finish).*exp(2*(S_short-S_M)*
        int_funct(n)))*delr)))-backscatter_M(n-start+1);
end
C = 521.63;

backscatter_64 = zeros(1,finish);
for n = start:finish
    backscatter_64(n) = (L_long(n))/((C*(TL(n)^2))-(2*S_long*(sum(L_long(n:finish)*delr))));
end

alpha_532 = backscatter_532 .* S_short;

alpha_64 = backscatter_64 .* S_long;
```

Signal to Noise Calculations

PMT Signal to Noise Calculation

```
alt = 0:20000; %altitude range [m] to use for calculation

h = alt;
T = 288.15 - (.006545.*h); %temp profile
p = ((288.15./T).^(-.034164/.006545)).*(1.013e5); %pressure profile
```

```
wav = 532; %wavelength [nm]
backscatter_M = (3742.8*(p./T)./(wav^4)).*10; % molecular backscatter
alpha_M = ((backscatter_M .*(8*pi))./3); %molecular extinction

S_M = mean(alpha_M/backscatter_M); %molecular extinction/backscatter
T2 = alt; %transmission through modeled molecular atmosphere to range r
for n = 1:20001
    T2(n) = exp(-2*sum(alpha_M(1:n)))./(n^2);
end

lambda = .000000532; %wavelength
quantum = .1; %quantum efficiency
h  = 6.626E-34 ; % Planck's
qe = 1.602E-19; %electron charge
c = 3*(10^8); %light speed
A = ((.279/2)^2)*pi; %telescope area
tau = .00000001; %pulse width [s] of laser
%E = .05;
delta_r = 1.5; %range bin [m]
bw = 100000000; %bandwidth of PMT [Hz]
Gain = 10^6; %gain of PMT
Power = (E * A * c  .* backscatter_M * .3 .* T2)./2; %power recieved
Idark = .000000001; %dark current
delta = 4; %gain of a single dynode stage
k = 1.38E-23;%Boltzmann
T = 273; %temperature [K]
RL = 50; %load resistance

Ip = (Power .* quantum .*lambda .* Gain .*qe)./(h*c); %photo-current

SNR1 = Ip./sqrt((2*qe*bw.*Ip * Gain).*(1/(1+ (1/delta)))+(4*qe*bw*Idark)+(4*k*T*bw/RL)); %signal
    to noise ratio

figure
hold on;
for n = [1  10  100 ]
SNR = sqrt(n)*SNR1; %adjusting for averaging 1,10,100 returns together
plot(SNR)
end
hold off;
%plot(T2);
```

APD Signal to Noise Calculation

```
alt = 0:20000; %altitude range [m] to use for calculation

h = alt;
T = 288.15 - (.006545.*h); %temp profile
p = ((288.15./T).^(-.034164/.006545)).*(1.013e5); %pressure profile

wav = 1064; %wavelength [nm]
backscatter_M = (3742.8*(p./T)./(wav^4)).*10; % molecular backscatter
alpha_M = ((backscatter_M .*(8*pi))./3); %molecular extinction
```

```
S_M = mean(alpha_M/backscatter_M); %molecular extinction/backscatter
T2 = alt; %transmission through modeled molecular atmosphere to range r
for n = 1:20001
    T2(n) = exp(-2*sum(alpha_M(1:n)))./(n^2);
end

Rapd = 5; %apd responsivity [A/W]
h  = 6.626E-34 ; %h
qe = 1.602E-19; %electron
c = 3*(10^8); %lightspeed
%E = .08;
A = ((.279/2)^2)*pi; %telescope area
tau = .00000001; %pulse duration [s]
Eo = .1; %energy of a single laser pulse
delta_r = 1.5; %1 range bin
bw = 100000000; %bandwidth of detector [Hz]
Gain = 100; %gain of detector
Power = (Eo * A * c  .* backscatter_M * .3 .* T2)./2; %power recieved
Idark = .0000000000001; %dark current
F = 2;   %excess noise factor
Ip = Power .*Rapd; %Signal current
k = 1.38E-23;%Boltzmann
T = 273; %temperature [K]
RL = 50; %load resistance

%SNR1 = Ip./sqrt((2*qe*bw.*Ip * Gain)+(4*qe*bw*Idark));
SNR1 = ((Ip.^2).*(Gain^2))./((2*qe.*(Idark + Ip).*bw.*(Gain^2).*F)+(2*qe*Idark)+(4*k*T*bw/RL)); %
    signal to noise ratio
figure
hold on;
for n = [1  10  100 ] %plot for averaging 1,10,100 returns together
SNR = sqrt(n)*SNR1;
plot(SNR)
end
hold off;
%plot(T2);
```

PMT Signal to Noise Calculation Including Quantization Noise

```
alt = 0:20000; %altitude range [m] to use for calculation

h = alt;
T = 288.15 - (.006545.*h); %temp profile
p = ((288.15./T).^(-.034164/.006545)).*(1.013e5); %pressure profile

wav = 532; %wavlength [nm]
backscatter_M = (3742.8*(p./T)./(wav^4)).*10; % molecular backscatter
alpha_M = ((backscatter_M .*(8*pi))./3); %molecular extinction

S_M = mean(alpha_M/backscatter_M); %molecular extinction/backscatter
T2 = alt; %transmission through modeled molecular atmosphere to range r
for n = 1:20001
```

```
    T2(n) = exp(-2*sum(alpha_M(1:n))./(n^2);
end

lambda = .000000532; %wavelength
quantum = .1; %quantum efficiency
h  = 6.626E-34 ; % Planck's
qe = 1.602E-19; %electron charge
c = 3*(10^8); %light speed
A = ((.279/2)^2)*pi; %telescope area
tau = .00000001; %pulse width [s] of laser
%E = .05;
delta_r = 1.5; %range bin [m]
bw = 100000000; %bandwidth of PMT [Hz]
Gain = 10^6; %gain of PMT
Power = (E * A * c  .* backscatter_M * .3 .* T2)./2; %power recieved
Idark = .000000001; %dark current
delta = 4; %gain of a single dynode stage
k = 1.38E-23;%Boltzmann
T = 273; %temperature [K]
RL = 50; %load resistance

Ip = (Power .* quantum .*lambda .* Gain .*qe)./(h*c); %photo-current

SNR1 = Ip./sqrt((2*qe*bw.*Ip * Gain).*(1/(1+ (1/delta)))+(4*qe*bw*Idark)+(4*k*T*bw/RL)); %signal
    to noise ratio

sigma = var(Ip.*RL); %variance of data
B = 14-1;%number of bits -1
X = 5; %full voltage range of A/D /2
SNR2 = 10*log((12*(2^(2*B))*(sigma^2))/(X^2)); %quantization SNR

figure
hold on;
for n = [1   10   100 ]
SNR = sqrt(n).*(1./((1./SNR1)+(1/SNR2))); %combine 2 SNR measurements
plot(SNR)
end
hold off;
%plot(T2);
```

APD Signal to Noise Calculation Including Quantization Noise

```
alt = 0:20000; %altitude range [m] to use for calculation

h = alt;
T = 288.15 - (.006545.*h); %temp profile
p = ((288.15./T).^(-.034164/.006545)).*(1.013e5); %pressure profile

wav = 1064; %wavlength [nm]
backscatter_M = (3742.8*(p./T)./(wav^4)).*10; % molecular backscatter
alpha_M = ((backscatter_M .*(8*pi))./3); %molecular extinction

S_M = mean(alpha_M/backscatter_M); %molecular extinction/backscatter
```

```
T2 = alt; %transmission through modeled molecular atmosphere to range r
for n = 1:20001
    T2(n) = exp(-2*sum(alpha_M(1:n)))./(n^2);
end

Rapd = 5; %apd responsivity [A/W]
h  = 6.626E-34 ; %h
qe = 1.602E-19; %electron
c = 3*(10^8); %lightspeed
%E = .08;
A = ((.279/2)^2)*pi; %telescope area
tau = .00000001; %pulse duration [s]
Eo = .1; %energy of a single laser pulse
delta_r = 1.5; %1 range bin
bw = 100000000; %bandwidth of detector [Hz]
Gain = 100; %gain of detector
Power = (Eo * A * c  .* backscatter_M * .3 .* T2)./2; %power recieved
Idark = .0000000000001; %dark current
F = 2;   %excess noise factor
Ip = Power .*Rapd; %Signal current
k = 1.38E-23;%Boltzmann
T = 273; %temperature [K]
RL = 50; %load resistance

%SNR1 = Ip./sqrt((2*qe*bw.*Ip * Gain)+(4*qe*bw*Idark));
SNR1 = ((Ip.^2).*(Gain^2))./((2*qe.*(Idark + Ip).*bw.*(Gain^2).*F)+(2*qe*Idark)+(4*k*T*bw/RL)); %
    signal to noise ratio

sigma = var(Ip.*RL); %variance of data
B = 14-1;%number of bits -1
X = 5; %full voltage range of A/D /2
SNR2 = 10*log((12*(2^(2*B))*(sigma^2))/(X^2)); % quantization noise SNR

figure
hold on;
for n = [1   10   100 ]
SNR = sqrt(n).*(1./((1./SNR1)+(1/SNR2))); %combined SNR for 1,10,100 shots
plot(SNR)
end
hold off;
%plot(T2);
```